Fluids in porous media: a morphometric approach

2005 J. Phys.: Condens. Matter 17 S503

(http://iopscience.iop.org/0953-8984/17/9/014)

INSTITUTE OF PHYSICS PUBLISHING JOURNAL OF PHYSICS: CONDENSED MATTER

J. Phys.: Condens. Matter **17** (2005) S503–S534 doi:10.1088/0953-8984/17/9/014

Fluids in porous media: a morphometric approach

Klaus Mecke[1,3] **and C H Arns**[2]

[1] Institut für Theoretische Physik, Universität Erlangen-Nürnberg, Staudtstrasse 7, 91058 Erlangen, Germany
[2] Department of Applied Mathematics, Research School of Physical Sciences and Engineering, Australian National University, Canberra ACT 0200, Australia

E-mail: klaus.mecke@physik.uni-erlangen.de

Received 24 November 2004
Published 18 February 2005
Online at stacks.iop.org/JPhysCM/17/S503

Abstract

Predicting the relationship between the morphology of porous media and their physical properties, e.g, the conductivity, elasticity and permeability, is a long-standing problem and important to a range of applications from geophysics to materials science. Here, a set of four morphological measures, so-called Minkowski functionals, is defined which allows one to quantitatively characterize the shape of spatial structures, to optimally reconstruct porous media, and to accurately predict material properties. The method is based on integral geometry and Kac's theorem which relates the spectrum of the Laplace operator to the four Minkowski functionals. Analytic expressions for mean values of Minkowski functionals in Boolean models allow the definition of an effective shape of a grain in a system made up of a distribution of arbitrarily shaped constituents. Reconstructing the microstructure using this effective grain shape leads to an excellent match to the percolation thresholds and to the mechanical and transport properties across all phase fractions. Additionally, the use of the effective shape in effective medium formulations leads to good explicit predictions of bulk moduli. The method is verified for several model systems and sedimentary rock samples, demonstrating that a single tomographic image is sufficient to estimate the morphology and physical properties such as permeabilities and elastic moduli for a range of porosities.

Also the thermodynamic behaviour of fluids in porous media, i.e., the shape dependence of the grand canonical potential and of surface energies of a fluid bounded by an arbitrarily shaped convex pore, can be calculated in the thermodynamic limit fully from the knowledge of the Minkowski functionals, i.e., of only four morphometric measures. This remarkable result is based on Hadwiger's theorem on the completeness of the additive Minkowski functionals and the assumption that a thermodynamic potential is an 'additive' functional which can be understood as a more precise definition for the conventional term 'extensive'. As a consequence, the surface energy and other thermodynamic

[3] Author to whom any correspondence should be addressed.

0953-8984/05/090503+32$30.00

quantities contain in the thermodynamic limit, beside a constant term, only contributions linear in the mean and Gaussian curvature of the pore and not an infinite number of curvature terms. Finally, starting from a microscopic density functional for an inhomogeneous fluid in a porous medium the phase coexistence (capillary condensation) and the critical point of the fluid is determined in terms of structure functions and morphological measures of the pore space and calculated explicitly for specific random porous structures using results from integral geometry.

(Some figures in this article are in colour only in the electronic version)

1. Introduction: predicting physical properties of porous materials

The characterization and realistic modelling of disordered porous materials as diverse as soils, sedimentary rocks, paper and catalysts has been a major problem for physicists, earth scientists and engineers for many years [1–4]. Nevertheless, the prediction of mechanical and optical properties of the material, as well as the prediction of transport and phase behaviour of fluids in porous structures, from measures of the morphology and topology is still an unsolved problem. The complicated pore structure of an interconnected three-dimensional network of capillary channels of nonuniform sizes and shapes distinguishes a porous medium from any other solid or planar substrate.

How do we characterize the structure of a complex material? This question is both of fundamental interest and is crucial to the understanding of many industrially important processes. The statistical characterization and modelling of disordered microstructures is a central problem in several applied fields. Accurate modelling relies on the availability of good microstructural models, which in turn relies on accurate statistical characterization. In section 2 statistical measures are introduced which are sensitive to the morphology of structures [5]. A porous substrate may be modelled by overlapping grains (Boolean grain model; see [6]) and is characterized by structure functions and morphological measures such as volume, surface area, mean curvature, and connectivity of the pores. These measures are known as Minkowski functionals in integral geometry which provides powerful theorems to make the calculus convenient. In sections 3 and 4 these morphological measures are used to predict two important properties of fluids in porous media: transport and thermodynamic phase behaviour, respectively. Although results are preliminary they illustrate the possibilities of the morphological approach to study fluids in porous media as described in this paper.

In a first step the Minkowski functionals are used in section 2 to characterize, discriminate and finally reconstruct different complex material microstructures. The section mainly reviews the results from [7–10] and follows the presentation used there but has added new data of a Fountainebleau sandstone which supports the previous results. Three distinct classes of digitized complex microstructure are considered: particle based composites with different grain shapes, structures generated by level-cuts through Gaussian fields, and models based on a Voronoi tesselation of space [7, 8]. The models are chosen to represent a wide range of composite structure. Also several experimental data sets of a Fontainebleau sandstone are used which are generated from x-ray-CT imaging. The section illustrates first how the Minkowski functionals can discriminate different classes of structure (section 2.3; [8]). Next a reconstruction scheme for spatially complex structures is developed. It is shown that for *any* structure, one can, from a single image of a system at any phase fraction (porosity) define a set of parameters based on Minkowski functionals which allows one to accurately reconstruct the

medium for *all other* phase fractions (section 2.4; [8, 9]). Third, the morphometric approach is extended via the application of erosion and dilation operations. The method is used to sensitively discriminate between different morphologies (section 2.5; [10]).

The method introduced in section 2.4 allows one to define in section 3 an effective local shape of a grain from any complex system made up of a distribution of arbitrarily shaped constituents. The method requires no prior knowledge of the original ensemble of grain size and shape. Kac [11] showed that the short time behaviour of the diffusion equation in a complex porous medium is governed by four additive Minkowski measures defined by integral geometry. In section 3 it is shown that a reconstructed porous medium based on the equivalent shape which honours these additive measures exhibits similar physical properties to the original system [9]. In section 4 first steps are made towards the connection of the two main features, morphology and interfacial properties such as surface energies and wettability, in order to predict the phase behaviour of fluids in porous media.

2. Characterization and reconstruction of porous media

The structure of a disordered material—an oil bearing rock, a piece of paper, or a polymer composite—is a remarkably incoherent concept. Despite this, scientists and engineers are asked to predict the properties of a disordered material based on the 'structure' of its constituent components. A major shortcoming in the understanding of processes involving complex materials has been an inability to accurately characterize microstructure. The specification of 'structure' requires topological as well as geometric descriptors to characterize the connectivity and the shape of the spatial configuration. Oil recovery from petroleum reservoir rocks depends crucially on the topology of the pore space and on the mean curvature of the surfaces where immiscible phases meet at a contact angle. To determine accurate flow models and to devise intelligent recovery strategies requires an accurate characterization of reservoir rocks in terms of topology and geometry.

The models for stochastic geometries, which are considered in the literature to reconstruct porous media, can be loosely separated into three different classes:

(i) particle based models or so-called Boolean models, which include Poisson distributed overlapping oblate and prolate spheroids (see figure 1);
(ii) Gaussian models where interfaces are generated by level cuts of a superposition of random plane waves [12, 13]. Originally developed to describe the morphologies associated with spinodal decomposition [14], and later to describe the structure of bicontinuous microemulsions [15], the levelled wave model accounts for many features observed in real disordered materials [12] including amorphous composite, polymer blends [16] and foams [17]. An examples of the morphologies which can be generated by level cuts of Gaussian models is illustrated in figure 2(a).
(iii) The third class of morphologies, random cellular solids [18], is constructed using a Voronoi tesselation. In this model the space is subdivided randomly into convex polyhedra by scattering Poisson points to a given density and construct the corresponding Wigner–Seitz cells, i.e., the bisecting planes between each pair of points. Within each polyhedron every point is closer to the given Poisson point than to any other. The resultant structure is similar to that of a closed-cell foam (see figure 2(b); thickening the facets) or to aerogels (see figure 2(c); thickening of edges).

To date, the main toolkit used to quantify such complex structures has been primarily that of the statistical physicist and not the advanced techniques developed in spatial statistics [2, 19–21] and digital image analysis [22]. Complete characterization of the effective morphology

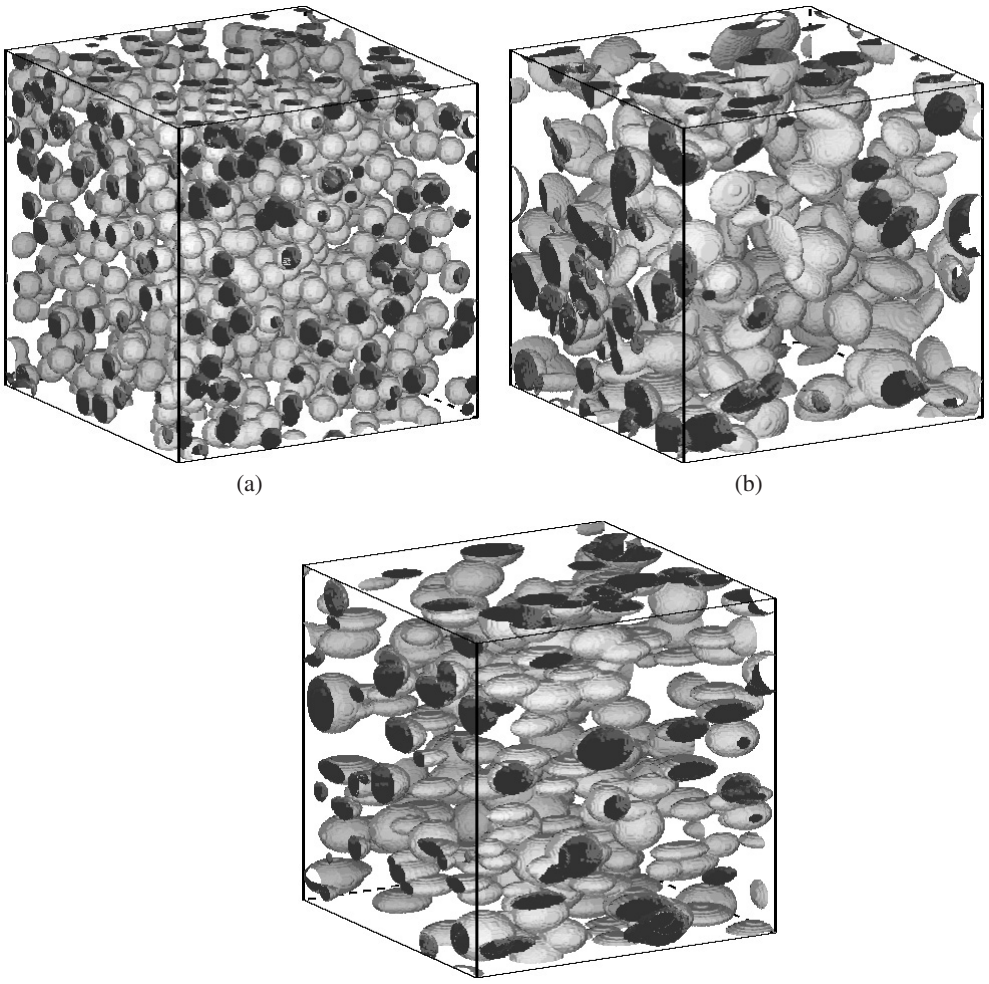

Figure 1. The interface of various Boolean models where overlapping convex grains (particles) are distributed randomly (from [10]): (a)–(c) overlapping spheres, overlapping spheroids randomly oriented and overlapping spheroids, fully aligned. The volume fraction of the particle phase is $\phi = 0.2$.

however requires knowledge of an infinite set of n-point statistical correlation functions. In practice only lower order morphological information is available; common methods [23] are based on matching the first two moments (volume fraction and two-point correlation function) of the binary phase function to a random model. It is widely recognized that although the two-point correlation function of a reference and a reconstructed system is in good agreement, this does not ensure that the structures of the two systems will match well and attempts to reconstruct materials from experimentally measured two-point information have not been very successful [24, 25]. In addition, the function does not capture important features of the microstructure which are relevant for physical properties.

Other useful two-point characterizations of microstructure include the chord-length distribution function [22, 26] (and the related lineal-path function [27]), the pore size distribution function [28] and other techniques from spatial statistics and image

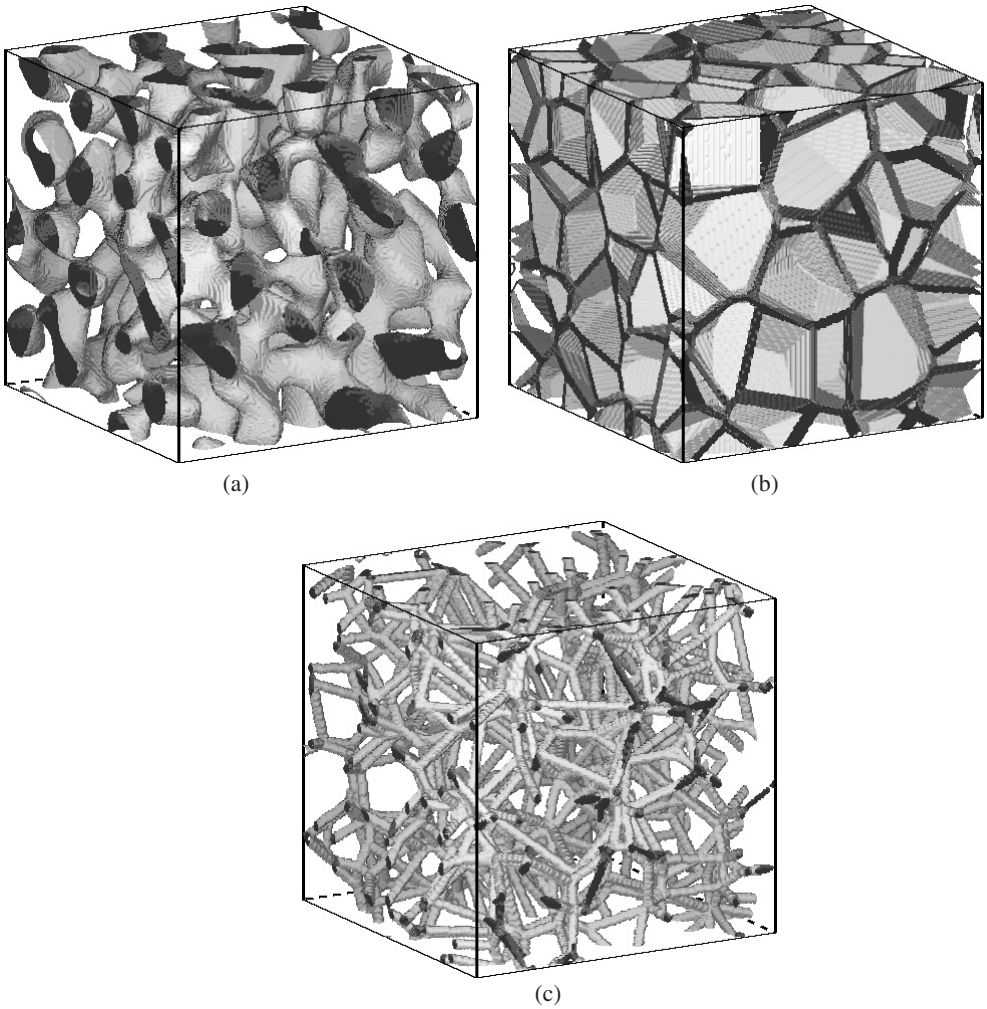

Figure 2. Stochastic geometries: (a) the interface of a Gaussian model (one-level cut) for volume fraction $\phi = 0.5$; (b) the interface of a Voronoi model with 100 seed points (facet model) and volume fraction $\phi = 0.25$ and (c) edge model for open cell foams at volume fractions of $\phi = 0.06$.

analysis [2, 22, 29, 30]. However, reconstructions of experimental data sets based on these characterizations have been shown to give a poor representation of the connectivity of the systems [31]. Functions that may provide more complete information about connectivity [33] are unfortunately too complex to incorporate into reconstruction schemes [31]. Incorporation of three- and four-point information may lead to a better estimation of structure, but their measurement is very complex and it is not clear how to incorporate the information within reconstruction algorithms. There is a need for morphological measures which include higher-order correlations, but are fast and reliable for characterizing the morphology of a structure.

Statistical measures which are sensitive to the morphology or shape of structures, i.e., to curvatures and connectivity, have been extensively investigated in other fields such as image analysis and pattern recognition [2, 22, 29, 30, 34]. Integral geometry [35, 36, 5, 37, 38]

provides a suitable family of morphological descriptors, the Minkowski functionals (MFs). These measures embody information from every order of the correlation functions in an integral way, are numerically robust even for small samples and yield global as well as local morphological information. One of the Minkowski functionals is the Euler characteristic which can be used as a topological measure for the connectivity of spatial structures. The Minkowski functionals characterize not only the connectivity, but the shape and content of spatial figures. In three dimensions the functionals are related to the familiar measures of volume fraction, surface area, integral mean curvature and Euler characteristic. These measures are efficiently calculated at the local scale from digital images [5, 38, 39]. Minkowski functionals have been used previously to distinguish quantitatively between different complex morphologies, to characterize turbulent and regular Turing patterns from chemical reaction-diffusion systems [40], to characterize spinodal decomposition and dewetting of thin liquid films [41–43], to discriminate between different cosmological models of the early universe [37, 44, 45] and to show that the hole distribution in thin films is inconsistent with the concept of spinodal decomposition, but consistent with a nucleation scenario [46–48]. Measurements of the Minkowski functionals for model random materials hves to date been made systematically on Boolean models and on two sandstone samples [7–10].

2.1. Integral geometric measures

Integral geometry [35, 36] provides complimentary methods and tools for measuring spatial structure. These tools are commonly used in other disciplines (e.g., digital image analysis [34]) but have only recently been developed in a systematic way as measures of complex media [7]. A family of measures, the Minkowski functionals in particular seem to be promising measures for describing the morphology of complex materials. The functionals characterize not only the connectivity, but the shape and content of spatial figures such as the configurations shown in figures 1–4 and 12. As many physical phenomena depend essentially on the geometry of the spatial structure, integral geometry may provide useful tools to study physical systems. In particular, integral geometry provides powerful formulae for the Boolean model. A review of these measures and applications in physics are given in [5, 38, 7].

The reconstruction method is based on Hadwiger's theorem [35, 36]; the *global* morphology of a two-phase complex material defined by the phase fraction ϕ, the surface area S, the integral mean curvature H and the genus χ is unique and forms the only motion-invariant and additive measure of structure. The method is also based on the result that the global morphology (ϕ, S, H, χ) can be related to a Boolean process defined by local grains of volume V_0, surface area V_1 and integral mean curvature V_2 at a density ρ [5, 38]. In this section integral geometric measures are studied only of digitized representations of complex media, i.e., of a two-component medium filling a cubic volume $N = L^3$. A digitized set of either component can be described by a collection of voxels of compact (closed and bounded) convex sets. The global morphology of a Boolean model, i.e., of a structure $\cup_i K_i$ made up of individual overlapping grains K_i of number density ρ are [5, 38, 7]

$$\begin{aligned} v_0 &= \phi(\rho) &&= 1 - \mathrm{e}^{-\rho V_0} \\ v_1 &= \tfrac{1}{6} S(\rho) &&= \mathrm{e}^{-\rho V_0}(1 - \mathrm{e}^{-\rho V_1}) \\ v_2 &= \frac{1}{3\pi} H(\rho) &&= \mathrm{e}^{-\rho V_0}(-1 + 2\mathrm{e}^{-\rho V_1} - \mathrm{e}^{-\rho(2V_1+V_2)}) \\ v_3 &= \chi(\rho) &&= \mathrm{e}^{-\rho V_0}(1 - 3\mathrm{e}^{-\rho V_1} + 3\mathrm{e}^{-\rho(2V_1+V_2)} - \mathrm{e}^{-\rho(3V_1+3V_2+V_3)}), \end{aligned} \tag{1}$$

where ϕ is the particle phase fraction, S is the surface to volume ratio, H is the specific integral mean curvature and χ is the specific Euler characteristic (genus). The $V_i = V_i(K)$ are the

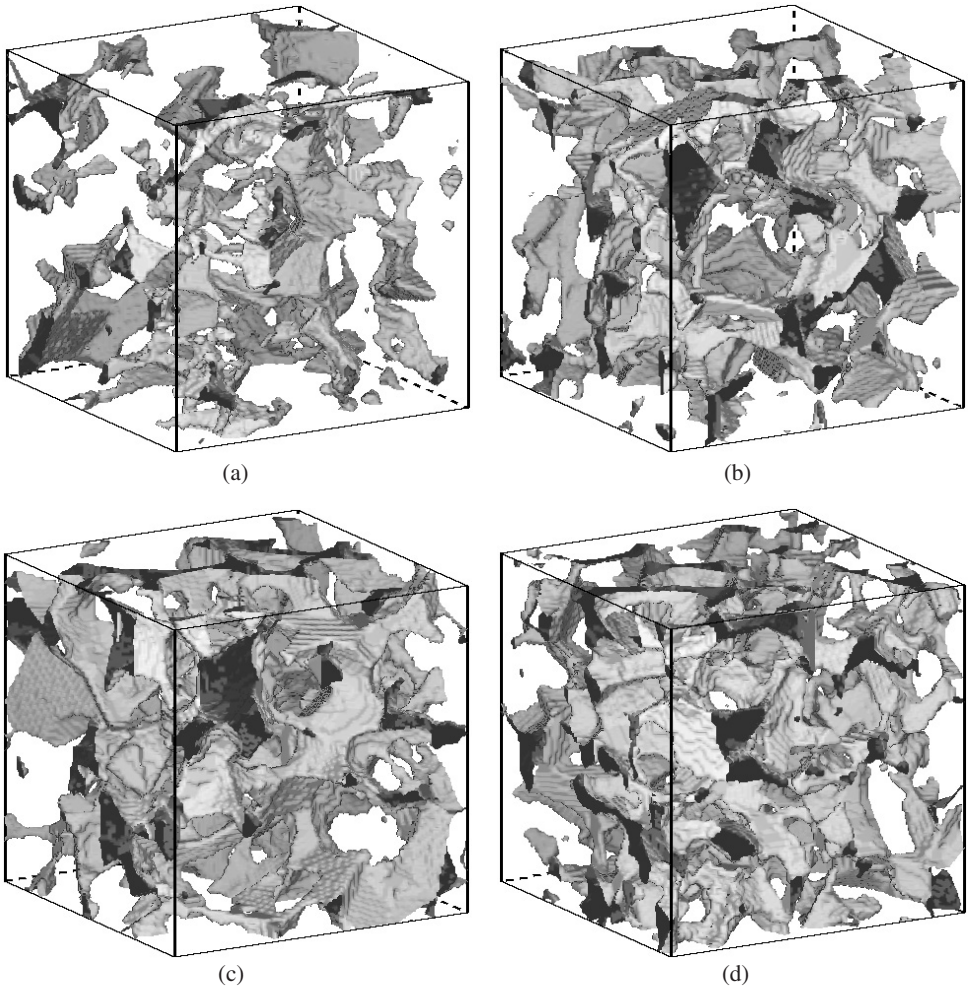

Figure 3. Pore space images of a central 120^3 piece of each of the four 480^3 Fountainebleau sandstone samples ((a) $\phi = 7.5\%$, (b) $\phi = 13\%$, (c) $\phi = 15\%$, (d) $\phi = 22\%$), each taken from the centre.

measures of the individual grains in units of the voxel size ($V_\mathrm{i} = 1$ for a single voxel), whereas the v_i denote the intensities of the measures $V_\mathrm{i}(\cup_\mathrm{i} K_\mathrm{i})$, i.e., the mean values of the Minkowski functionals of the union of all grains normalized by the total number of voxels. Note that these intensities were derived by Miles (1976) for *non*-discretized configurations (see [49] for an algorithm to numerically estimate $V_\mathrm{i}(\cup_\mathrm{i} K_\mathrm{i})$, and [50] for analytic expressions for the second order moments of $V_\mathrm{i}(\cup_\mathrm{i} K_\mathrm{i})$), whereas equation (1) holds for unions of digitized grains K defined as a collection of voxels. It is convenient to normalize the Minkowski functionals for digitized data so that for a single voxel one has $V_\mathrm{i} = 1$, in contrast to the normalization $W_\mathrm{i} = \omega_\mathrm{i} V_\mathrm{i}$ usually applied for shapes in the Euclidean space with the volume ω_i of an i-dimensional unit sphere. Thus, for cubes of sidelength λ voxels in three dimensions one has $V_0 = \lambda^3$, $V_1 = \lambda^2$, $V_2 = \lambda$ and $V_3 = 1$, and for lattice-aligned rectangular sticks of edge length $\lambda_\mathrm{i} V_0 = \lambda_1\lambda_2\lambda_3$, $V_1 = (\lambda_1\lambda_2 + \lambda_1\lambda_3 + \lambda_2\lambda_3)/3$, $V_1 = (\lambda_1 + \lambda_3 + \lambda_3)/3$ and $V_3 = 1$. These powerful formulae given in equation (1) illustrate that it is sufficient to know the morphology

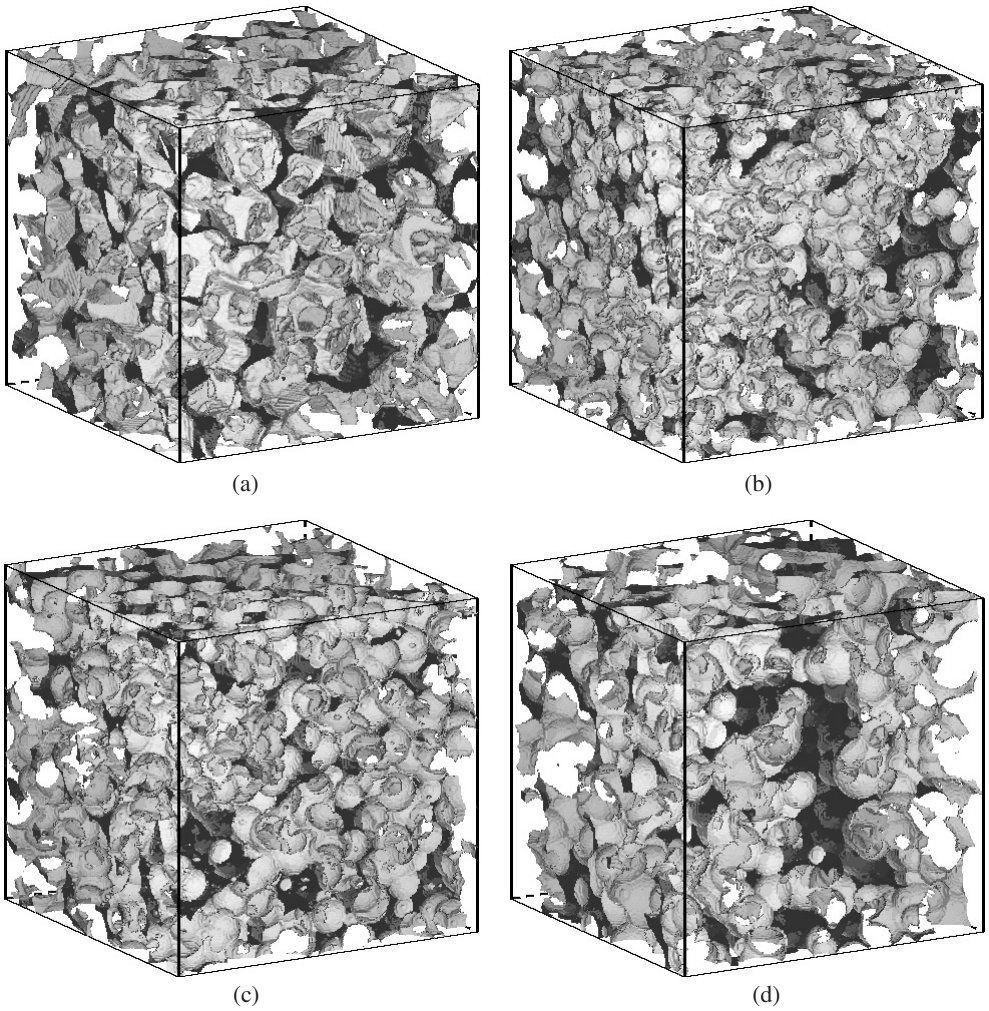

Figure 4. Visual comparisons of reconstructions to a 240^3 subset of the original Fountainebleau sandstone sample ($\phi = 15\%$): (a) Fountainebleau sandstone, (b) identical overlapping sphere model ($\mathrm{IOS}^{\mathrm{C}}$), (c) randomly oriented spheroids $\mathrm{ROS}^{(2)}$, (d) OSC.

of the individual grains $V_{\mathrm{i}} = V_{\mathrm{i}}(K)$ and the density of the grains ρ to derive the mean values v_{i} of the global morphology, measured in terms of ϕ, S, H and $\chi(\rho)$.

This result also holds for complex mixtures of grains where V_ν is now replaced by proper averaged values of arbitrarily shaped grains, for instance, for mixtures of polyhedra as used later. One can replace the quantities V_ν of a single grain by averages over an ensemble of n grains, weighted by the probability p_j of their occurrence $\langle V_\nu \rangle = \sum_{j=1}^{n} p_j V_{\nu j}$ for $\nu = 0, \ldots, d$ where $p_j = \rho_j/\rho$ is the ratio of the densities of the Poisson processes. The equation (1) also holds if the grains are correlated (hard-shell, soft-shell models) if one uses local measures $V_\nu[\xi(\vec{r})]$, which exhibit a small dependence on the correlation function $\xi(\vec{r})$ for short-ranged correlations. Details and the explicit dependences are given on p 161 in [20]. For most practical applications, one may assume constant values of V_ν in equation (1) for arbitrarily shaped and correlated mixtures of grains.

The intensities $\phi, H, S, \chi(\rho)$ of the global Minkowski functionals can be measured directly from a single 3D tomographic image or from a pair of 2D serial sections of a complex material, i.e., from any image made up of discrete voxels. For example, the volume fraction ϕ of a phase is trivially obtained by dividing the number of voxels of that phase by the total number of voxels. The other functionals are obtained by considering the interface associated with the vertices of each voxel. Global measures $v_i = V_i(\cup_i K_i)/N$ for each configuration are obtained by configuration counts over all vertices on any voxellated structure after normalizing by the total number $N = L^3$ of vertices [7, 51, 52]. In [7] the algorithm used to calculate these measures was validated against equation (1) for a monodisperse grain ensemble and in [8] for an ensemble made up of mixtures of grains. From this measurement and equation (1) one can determine the local shape of an equivalent grain ensemble, V_ν, $\nu = 0, 1, 2$, and its density ρ which is described below in detail (section 2.3).

2.2. Experimental images from microtomography

Direct measurement of a 3D structure is now available via x-ray computed microtomography [53, 54]. These techniques provide the opportunity to experimentally measure the complex morphology of a range of materials in three dimensions at resolutions down to a few micrometres and lower. From this technology four 4.52 mm diameter cylindrical core samples of Fountainebleau sandstone are obtained with a resolution of 5.68 μm [53–55]. X-ray computed tomographic images of porous media are grey scale images, usually with a bimodal population apparent, one mode corresponding to the signal from the void space, the second to the signal from the grain space. A simple thresholding based on matching the predetermined porosity is often used to segment a tomographic image and to obtain a binary pore–solid image. Here, we use data from Lindquist based one a thresholding by indicator kriging [56]. The images are also corrected for noise by re-identifying the phase type of all isolated grain and void voxel clusters. These isolated voxels would otherwise have a strong effect on many morphological measures. Finally, from each of the binarized cylindrical plugs of the Fountainebleau sandstone with bulk porosities $\phi = 7.5\%$, 13%, 15% and 22% a centred 480^3 cubic subset was extracted for analysis corresponding to a volume of 20.3 mm^3 (see figure 3). The samples show the variability of shapes and structures observed in the Fontainebleau cores. Fontainebleau is considered very homogeneous, and considered a 'benchmark' of a homogeneous rock in the petroleum industry, but a plot of the porosity variations shows considerable variability on the local grain scale.

2.3. Characterization of a sandstone sample

The availability of 3D images has accelerated the development of computational tools to directly measure the stochastic nature of the porous materials and to construct realistic representations of the complex space [57, 58]. A number of statistical models have been proposed for reconstructing porous media from statistical information [23, 24, 59, 60]. These methods, based on different underlying model microstructures, are generated in such a manner that they match the observed two-point statistical properties of the rock (see p 93 in [19]). Of course, one can derive more complex model systems which incorporate other two-point correlation information, e.g., chord distribution functions [26, 22, 59], but recent work has shown that these measures give a poor representation of connectivity [31]. Results on Minkowski functionals of these more complex models indicate that this is reflected in a poor match to the curvature measures $v_2 \sim H$ and $v_3 \sim \chi$ [8, 10]. Let us compare the sandstone samples with several stochastic models.

(i) The first is based on a germ–grain model with spherical grains, the so-called 'identical overlapping sphere' (IOS^C) model. The correlation function for the phase external to the spheres of radius r_0 is $p^{(2)}(r) = \phi^{1+3r/(4r_0)-r^3/(16r_0^3)}$ for $r < 2r_0$ and $p^{(2)}(r) = \phi^2$ for $r > 2r_0$ with the surface to volume ratio $Sr_0 = -3\phi \ln \phi$. The parameter r_0 can be chosen to match best the two-point correlation functions of the sandstone samples which is indicated in the superscript (C).

(ii) Gaussian random field models are frequently used to reconstruct porous media. Here, we use configurations of a Gaussian model as introduced in [32], where five different one-level cuts of the same realization are intersected. To generate a matching Gaussian random field the field–field correlation function is employed where the length scale parameters are obtained by a best fit procedure to minimize the non-linear least squares error to the sandstone sample.

(iii) In Boolean models overlapping convex grains (particles) are distributed randomly. In the following section 2.4 a technique is presented to determine the shape of the grain, so that the morphologies of the sandstone samples are matched best. Three different types of grains are considered: (a) identical spheres ($IOS^{(V)}$ model), (b) a mixture of spheres with two different radii ($IOS^{(2)}$ model), and (c) a mixture of spheroids of different sizes, i.e., half-axes ($ROS^{(2)}$ model).

(iv) Alternative methods to generate a Boolean ensemble exist for model microstructures based on spheres. Recently Thovert *et al* [57] introduced a reconstruction technique for a sandstone based on a model of overlapping spheres where the sphere size distribution is defined by the probability density of the covering radius for spheres (OSC model). This method is employed to generate another appropriate Boolean model for the four sandstone images. The median a of the radius distributions defined in [57] is given in table 2.

The original sandstone microstructure for the sample at 15% and reconstructions via the overlapping grain models (IOS^C, $ROS^{(2)}$, OSC) are illustrated in figure 4. Visual inspection suggests that the $ROS^{(2)}$ and OSC models more closely resemble the original microtomographic image, but quantitative measures are definitely needed to distinguish these structures.

The quantities usually used to characterize the microstructure of these systems are the volume fraction, the surface to volume ratio S and the two-point correlation function $p^{(2)}(r)$. Note that $p^{(2)}(0) = \phi$, $p^{(2)}(\infty) = \phi^2$ and $S = -4\frac{\mathrm{d}p^{(2)}(0)}{\mathrm{d}r}$. The stochastic models that best match the four 480^3 samples are generated and the two-point correlation functions $p^{(2)}(r)$ of these models are compared in figure 5. The match of $p^{(2)}(r)$ is very good for the Gaussian intersection model and the overlapping sphere (IOS^C) model, where the two-point correlation function is used to determine the free parameters of the models. Thus, the good agreement is not astonishing. It is also not amazing that the Boolean model IOS^V shows large deviations, because $p^{(2)}(r)$ is never used in the construction of this model as explained in the following section 2.4. However, the Boolean model $ROS^{(2)}$ of a mixture of overlapping spheroids exhibits a remarkable agreement with the correlation function of the sandstone sample, although the model does not use this information. One may conclude that the correlation function is not a very sensitive measure to distinguish different stochastic structures.

Let us now compare the intensities v_i of the global Minkowski functionals for the various models and for the sandstone samples (figure 6). An analysis of the full 480^3 cubic subsets would only give a single value for the porosity of each of the four samples and would provide few data to compare to stochastic models. However, the samples are reasonably heterogeneous in the pore volume fraction ϕ. Due to this natural heterogeneity and by appropriately choosing different window sizes on the image it is possible to measure morphological parameters for the sandstone images across a range of pore volume fractions ϕ. This gives us a more

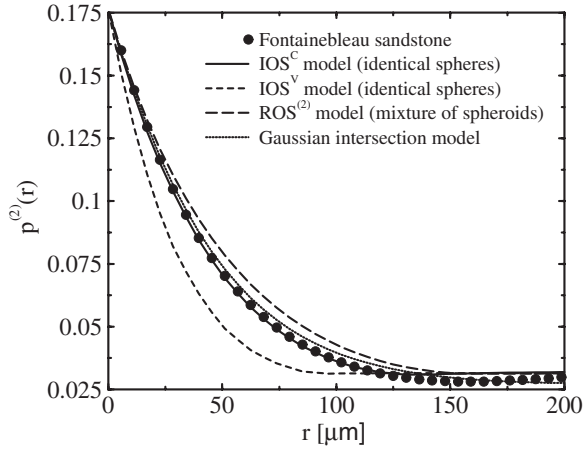

Figure 5. The two-point correlation function $p^{(2)}(r)$ of the 480^3 Fountainebleau sandstone sample and several reconstructed model structures (see figure 4) do not show significant differences, although they are based on completely different construction techniques. In contrast, the morphometric measures shown in figure 6 make differences in the models clearly visible.

comprehensive data set with which to compare experimental images to equivalent models. For the Fontainebleau samples cubic blocks of 480^3, 240^3 and 120^3 are considered. This provided in all cases a good spread of porosities across different sampling volumes. The measured morphological properties S, H, $\chi(\phi)$ resulting from the sampling window at 120^3 are summarized in figure 6. The values for the samples were binned in steps of porosity $\Delta\phi = 0.02$. It is interesting that the fourth Fontainebleau data set at 22% exhibits very different measures to the first three sets. This could indicate the potential presence of heterogeneity, as seen in figure 5(c) in Thovert *et al* [57]. Another explanation may be that another diagenetic process occured during consolidation of this sample.

The Gaussian intersection model does not satisfactorily match the experimental data (not shown), which indicates the granular structure of the sedimentary rock. The surface area $v_1 \sim S$ is matched by the identical overlapping sphere ($\mathrm{IOS^C}$) models, but the integral mean curvature $v_2 \sim H$ and the topology $v_3 \sim \chi$ is not described well by the $\mathrm{IOS^C}$ model. As indicated by the relative error in the local integral geometric measures V_i (table 2) the $\mathrm{ROS^{(2)}}$ model almost exactly matches the local measures of the sandstone samples. The $\mathrm{IOS^C}$ and OSC model perform poorly, particularly for H, where $\mathrm{IOS^C}$ overestimates and OSC underestimates the image data (see figure 6).

Even though the other models do reasonably well at the fraction where the two-point correlation functions were matched, they fail to describe the structure across a range of phase fractions. Different transport and mechanical processes will depend more strongly on the agreement with specific morphological measures. For example, single-phase flow and conductivity in clean sandstones will be most strongly affected by surface-to-volume ratio (related to average constriction size) and topology. A model which accurately describes these two measures may still yield good agreement with experiment. However, multiphase flow properties depend crucially on the curvature of the surfaces where immiscible phases meet. For these processes a model that also accurately matches H, i.e., v_2, will be required. In this case the $\mathrm{ROS^{(2)}}$ model is the best of the candidates as a reconstructed data set. In the following section we describe briefly how this model is constructed.

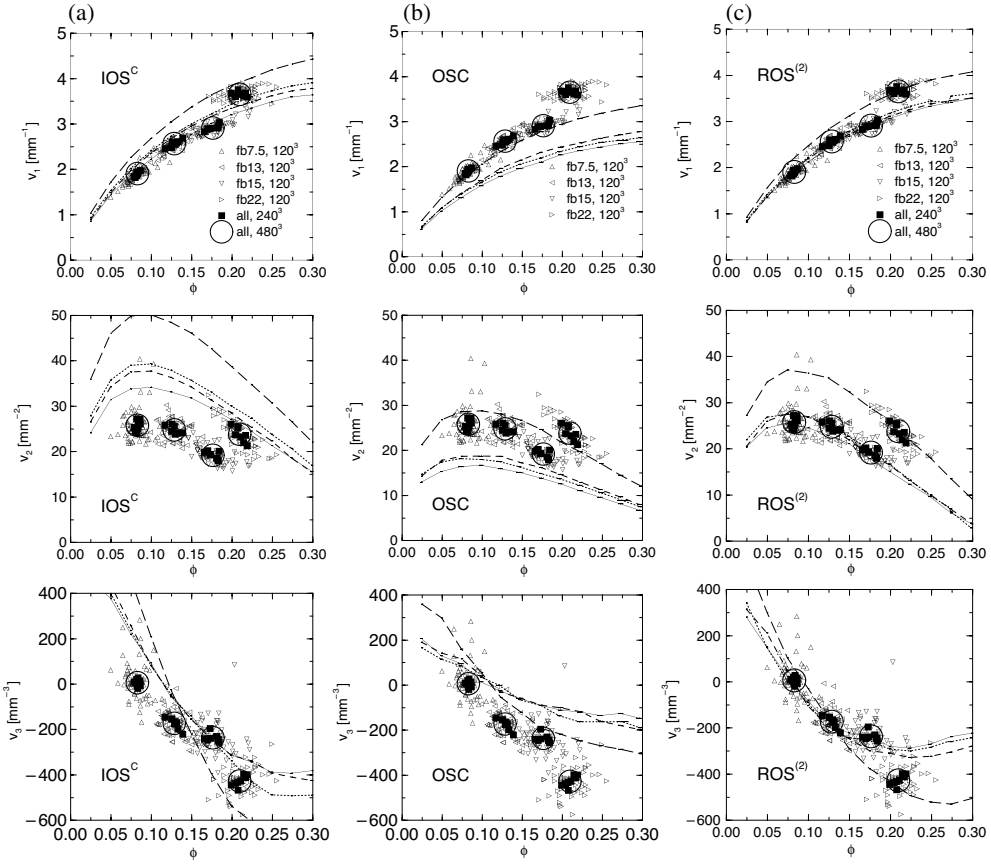

Figure 6. Comparison of the Minkowski functionals over fraction ϕ for each of the four Fontainebleau sandstone samples (symbols) to three stochastic models (from [8]): (a) (left) IOS$^{\mathrm{C}}$, (b) (middle) OSC and (c) (right) ROS$^{(2)}$. For $v_2 \sim H$ and $v_3 \sim \chi$ the measures for the highly connected neighbourhood are given. The curves show the binned Minkowski functionals of the reconstructed systems (solid, fb7.5; dotted, fb13; dashed, fb15; long dashed, fb22). Although the correlation functions are similar in the models (see figure 5), the morphometric measures differ considerably, indicating that the ROS$^{(2)}$ model matches best the sandstone structure.

2.4. Reconstruction of complex morphologies via Minkowski functionals

In the previous section the knowledge of the local 'grain' morphology V_{i} in equation (1) is used to predict the global morphology, i.e., the surface area S, the mean curvature H, and the Euler characteristic χ, of a Boolean model at any porosity. Now let us consider the inverse process; from a single snapshot of a complex structure one can derive an equivalent local 'grain' ensemble which will generate the same complex global morphology. As one can evaluate the four global morphological measures ϕ, S, H, χ from a single 3D image, one can use equation (1) to obtain estimates for V_0, V_1, V_2 and density ρ of the local grain morphology, which may finally be used to select the grains in a Boolean model for reconstruction. The local grain measures V_{i} of the Fontainebleau sandstone samples are summarized in table 1—estimated by inverting equation (1). Note that all Boolean models have convex grains with $V_3 = 1$. This technique is called 'method of intensities' (see p 89 in [19]) and statisticians consider it as the best estimation method. Here it illustrates the ability of the morphological approach to accurately reconstruct the experimental 3D

Table 1. Mean values of the local Minkowski functionals for the four Fontainebleau sandstone samples of size 480^3 given in section 2.2 ($V_3 = 1$ for convex grains).

Sample (%)	V_0 (10^{-3} mm^3)	V_1 (10^{-3} mm^2)	V_2 (mm)
7.5	0.4019	3.994	0.0473
13	0.3619	3.752	0.0466
15	0.4506	4.520	0.0523
22	0.3361	3.965	0.0509

microtomographic images of the sandstone. Of course, the microstructure of a sandstone is a result of a complex physical process, which can include consolidation, compaction and cementation of an original grain packing, and more realistic models of sandstones have been derived [62, 63]. These methods require, however, the simulation of the generating process including primary grain sedimentation followed by a diagenetic process such as compaction and cementation. This process is both computationally expensive and requires several fitting parameters. Reconstructing the microstructure of sandstones by the simple Boolean model may therefore not lead to an excellent match. However, a Boolean model with spherical grains has been proposed as a model which gives a reasonable representation of consolidated sandstone and yields good qualitative information on structure/property relationships. Moreover, also other work [57] has shown that the model of overlapping spheres gives a very good match to Fontainebleau sandstone data.

In the remainder of this section the reconstruction method based on the Boolean model is applied to the Fontainebleau sandstone sample described in section 2.2. The goodnesses of fit of three different Boolean models are compared: overlapping spheres with matching two-point information ($\mathrm{IOS}^{\mathrm{C}}$ model), the equivalent Boolean ensemble defined by local morphological measures V_{i} ($\mathrm{ROS}^{(2)}$ model) and a recent model (OSC) based on the probability density of covering spheres [57].

In the first approach the diameters for an overlapping grain model with a deterministic spherical grain are estimated by means of the two-point correlation function introduced in section 2.3 (identical overlapping sphere ($\mathrm{IOS}^{\mathrm{C}}$) model). In the second approach, the diameters are estimated based on the 'method of intensities', i.e., the single sphere can also be determined by using the reconstruction technique (see equation (1)) based on the local grain measures V_ν ($\mathrm{IOS}^{\mathrm{V}}$ model). The local grain measures of the Fontainebleau sandstone samples are given in table 1, and the best matching models to these local measures in table 2. Interestingly, the size of the best matching $\mathrm{IOS}^{\mathrm{V}}$ sphere is significantly smaller than the $\mathrm{IOS}^{\mathrm{C}}$ sphere.

To gain some degrees of freedom, a single equivalent spheroidal grain (randomly oriented spheroids ($\mathrm{ROS}^{(1)}$) model) is attempted to fit to the local V_ν given in table 1, but one observes only a slight improvement in the prediction. It is therefore necessary to use more complex models. Our first attempt is a Boolean model with a random mixture of spherical grains to accurately match the local measures. This is done first for a two-point diameter distribution, i.e., for two different spheres ($\mathrm{IOS}^{(2)}$). This leads to a better match, but the error in V_2 is still considerable (see table 2). Then the best two-particle match for a Boolean model of spheroids ($\mathrm{ROS}^{(2)}$ model) is derived. The match to the local V_ν of the experimental image is now excellent. It is interesting to note that the unique information obtained from the integral geometric measures leads to a quite complex equivalent stochastic model for the Fontainebleau sandstone. The $\mathrm{ROS}^{(2)}$ model is composed of two very different particle sizes (table 2). The median a of the radius distributions for the OSC model is given in table 2. This median is comparable to the size of the larger particles in the two-particle reconstructions but is significantly larger than either single-particle IOS fit.

Table 2. Parameters for the Boolean models of the Fontainebleau sandstone and errors of the morphological matches. The first IOS model (IOS^C) was matched using the void–void correlation function. The other models are matched using the reconstruction based on estimating the local grain shape, i.e. the morphometric functionals V_i, of a Boolean model. IOS is generalized to more than one sphere; all spheroids are randomly oriented (ROS model: randomly oriented spheroids). Note the large errors E_{V_i} in the local measures for the one-particle IOS model. For all two-particle models one of the particles is very small and has a width of the order of a few voxels. a, b, c note the length of the half-axes with the exception of the OSC model, where a notes the median of the radius distribution $G(r_c) = 1/2$.

Model	Core (%)	p	a (μm)	b (μm)	c (μm)	E_{V_0}	E_{V_1}	E_{V_2}
IOS^C	7.5	1	71.3			3.4	3.6	2.5
	13	1	65.8			2.4	2.6	1.8
	15	1	69.1			3.1	3.4	2.5
	22	1	59.0			1.6	1.8	1.3
IOS^V	7.5	1	45.8			5.3×10^{-3}	0.71	0.022
	13	1	44.6			0.016	0.66	6.8×10^{-3}
	15	1	47.4			4.1×10^{-3}	0.058	0.84
	22	1	43.2			2.5×10^{-3}	0.44	0.67
$IOS^{(2)}$	7.5	0.865	16.6			4.8×10^{-3}	6.6×10^{-4}	0.022
		0.135	88.3					
	13	0.864	16.6			3.9×10^{-5}	1.8×10^{-4}	6.8×10^{-3}
		0.136	84.8					
	15	0.817	13.3			7.5×10^{-5}	1.1×10^{-4}	0.018
		0.183	83.3					
	22	0.798	16.5			2.2×10^{-5}	3.0×10^{-4}	8.7×10^{-3}
		0.202	72.4					
$ROS^{(2)}$	7.5	0.848	12.5	11.9	8.52	1.5×10^{-7}	7.5×10^{-6}	1.5×10^{-4}
		0.152	83.5	80.7	77.2			
	13	0.863	15.9	11.4	9.09	9.1×10^{-8}	5.4×10^{-7}	3.0×10^{-5}
		0.137	84.6	76.7	76.1			
	15	0.794	15.3	12.5	8.52	1.8×10^{-7}	2.7×10^{-6}	8.9×10^{-5}
		0.206	84.6	80.1	76.7			
	22	0.751	16.5	10.8	8.52	2.1×10^{-7}	2.0×10^{-6}	1.6×10^{-5}
		0.249	74.4	67.0	63.6			
OSC	7.5		94.8			7.4	5.2	2.4
	13		86.0			12	8.6	4.1
	15		85.9			5.3	3.9	2.0
	22		67.7			3.2	2.4	1.4

Studying table 2 and figure 6 one may conclude that the closest morphological match to the original data is given by the Boolean reconstruction technique over a range of porosity. The $ROS^{(2)}$ model matches all Minkowski functionals very well, $IOS^{(2)}$ is still good with the exeption of the V_3 measure, while $IOS^{(V)}$ is still better than the techniques based on two-point information ($IOS^{(C)}$) or covering spheres (OSC). In general, the reconstruction based on integral geometric measures of a Boolean model gives a better match to the morphology than the commonly used IOS^C and the recently developed OSC model. Moreover, unlike the IOS^C and OSC models, the current method is not limited to spherical grains, but can be used to generate more complex grain shapes. The morphological reconstruction of sandstones via Boolean models does not give as accurate a match to the experimental data as we observe when reconstructing a complex Boolean model by a simpler Boolean model. Clearly, a Boolean process cannot mimic sandstone formation (sedimentation, diagenesis, compaction, etc). The

reconstruction method can be improved: one development that will further highlight the utility of the proposed technique is based on conditioning the equivalent ensemble to better mimic the local morphology of the medium. This could be done by conditioning to local curvature measures or chord-length distribution measurements which will limit the choice of grain 'shape' to use in the equivalent Boolean ensemble. In oil recovery from petroleum reservoir rocks recovery depends crucially on the mean curvature of the surfaces where immiscible phases meet at a contact angle. Conditioning an equivalent Boolean ensemble to exhibit the same distribution of local mean curvature should lead to a better prediction of multiphase flow properties on reconstructed images. The current work is based on deriving equivalent local measures from an image for Boolean models: equation (1). Concluding, we emphasize that the morphometric reconstruction scheme provides much more information on the local structure of a sample than two-point correlation functions. Extension of the methodology to more general systems; hard-sphere mixtures, soft-sphere models and models based on Gaussian random fields representing a wider range of complex materials including ceramics, composite materials and fibrous media is now being considered. The technique can also be extended by applying the concept of parallel surfaces as described in the following section.

2.5. Characterization by parallel surfaces

In the previous section morphological measures were applied for the characterization and reconstruction of the shape of disordered systems. An even more powerful discriminator of morphology is based on the evolution of the Minkowski functionals $v_\nu(\epsilon)$ during erosion and dilation operations [64]. This methology has been used previously to discriminate between different cosmological models of the early universe [37, 44, 45] and to characterize the dewetting and structure formation in thin liquid films [46–48]. In these cases, the Minkowski functionals of parallel bodies of a point pattern (a convex set) were considered. The point pattern was dilated to obtain detailed morphological information where the parallel distance ϵ was used as the diagnostic parameter [49]. Here, the evolution of the Minkowski functionals is studied during erosion and dilation operations on complex *non-convex* morphologies [10]. The method can be used to discriminate morphology from 1D (chord-length), 2D (micrographs), and 3D (tomographs) data sets and the combination of parallel sets with Minkowski functions leads to a very accurate discrimination of morphology.

One can define the parallel body $A_\epsilon = \{\vec{x}|d(A,\vec{x}) \leqslant \epsilon\}$ of a structure A as the set of all points $\vec{x}$ with distances $d(A,\vec{x})$ less than ϵ to A. Here, $d(A,\vec{x}) = \min(|\vec{x}-\vec{y}|;\ \vec{y} \in A)$ denotes the minimal Euclidean distance where $|\vec{x}|$ is the standard norm in a d-dimensional Euclidean space. Changing ϵ corresponds to dilation $\epsilon > 0$ and erosion $\epsilon < 0$ of the spatial structure A. For negative values of ϵ the parallel body is defined formally by $A_{\epsilon<0} = \{\vec{x};\ d(A^c,\vec{x}) \leqslant \epsilon\}^c$, i.e., as the complement set of all points with distances less than ϵ to the complement A^c of A. Alternatively, one may define the parallel body $A_\epsilon = \cup_{\vec{x}\in A} B_\epsilon(\vec{x})$ by the union of all spheres $B_\epsilon(\vec{x})$ of radius $\epsilon > 0$ and centres $\vec{x} \in A$ inside A. For $\epsilon < 0$ the parallel body is given by the set of all centres $\vec{x}$ so that the union $A = \cup_{\vec{x}\in A_\epsilon} B_\epsilon(\vec{x})$ equals A. However, a direct implementation of this definition is computationally very inefficient as it requires one to place spheres of different sizes along all voxels at the interface at each erosion/dilation step. Parallel sets of non-convex spatial configurations are shown in figures 1 and 2: (A) the parallel body A_ϵ of distance ϵ of Poisson distributed points is the Boolean model of overlapping spheres of radius ϵ; the parallel body of facets (B) and edges (C) of a Voronoi tessellation yields completely different spatial structures and Minkowski functionals $v_\nu(\epsilon) = V_\nu(A_\epsilon)/N$ as functions of ϵ [7]. Parallel surface may not only be used to characterize spatial non-convex patterns such as point distributions, foams, gels, fractals or chemical patterns (see [5, 38–40]), but also to define

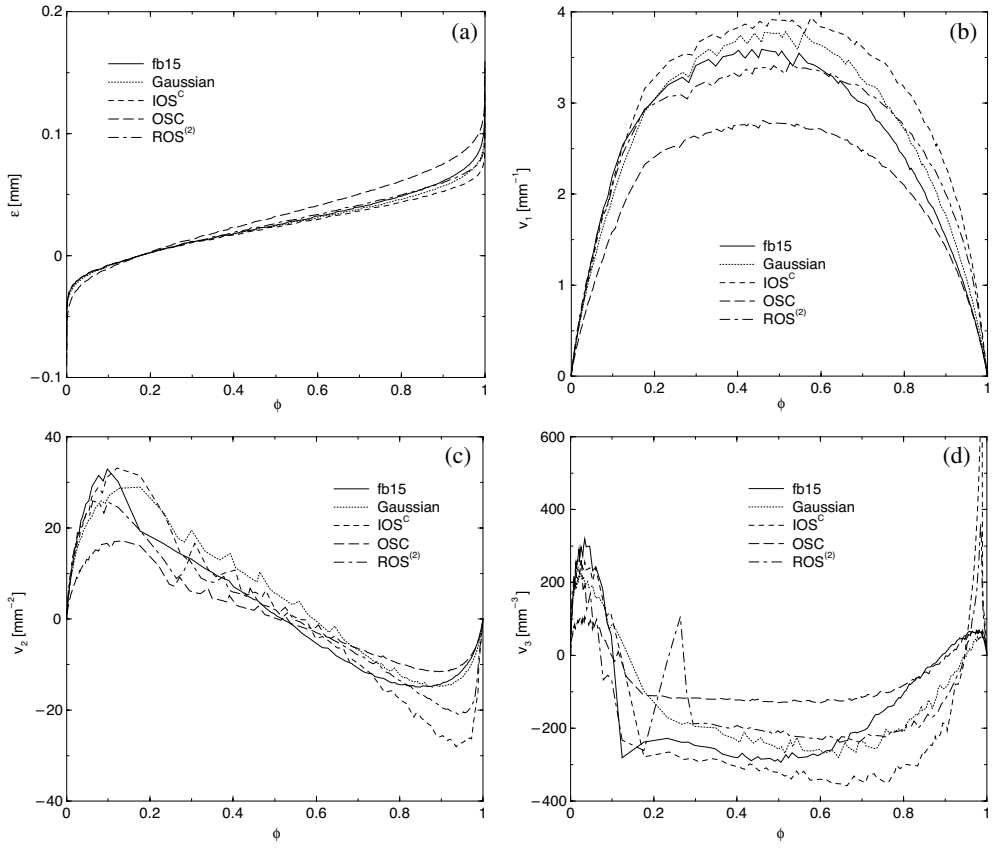

Figure 7. Minkowski functions $v_\nu(\epsilon)$ of the parallel surface at distance ϵ for the Fontainebleau sandstone, a Boolean model of overlapping spheres ($\mathrm{IOS^C}$), mixtures of ellipsoids ($\mathrm{ROS^{(2)}}$), a Gaussian random field and the OSC model as functions of the porosity $\phi(\epsilon)$.

appropriate stochastic models for porous media, network models for percolation and liquid wetting layers near substrates, which is important for fluids in porous media (see section 4.2).

To illustrate the powerful discrimination of morphology which comes from measuring the Minkowski functions of parallel bodies, figure 7 shows the Minkowski functions $v_\nu(\epsilon)$ of the parallel body (distance ϵ) of five different configurations: (A) Boolean model of overlapping spheres; (B) a mixture of spheroids; (C) a Gaussian random field; (D) the OSC model and (E) a sandstone—a real porous material. The three-dimensional structures are digitized on a 128^3 lattice and lengths are given in units of the pixel size [7]. The Minkowski functions $v_\nu(\epsilon)$ as functions of the volume $\phi(\epsilon)$ of the parallel body are completely different for the four spatial structures and none of the models can reproduce the functions for the sandstone.

The application of the parallel surface method to experimental data of Fontainebleau sandstone [8] shows that, while the reconstruction models considered work reasonably, none stands out as 'brilliant'—and more realistic morphologies need to be considered to get a good match as in [8] for model composites. This is left as future work, where process based models will be considered as developed in [65]. Nevertheless, this section 2 illustrates that the Boolean model is suitable for characterization and reconstruction of porous media such as sandstones. In the following, applications on transport properties (section 3) and phase behaviour (section 4)

are given to illustrate the possible impact of morphological measures and the Boolean model on predicting physical properties of porous media.

3. Fluid flow and elastic properties of porous media

In the previous section it was shown how an accurate stochastic reconstruction of a complex material made up of discrete pores or grains (inclusions) can be derived from a single 3D snapshot at any phase fraction. The method, based on integral geometric measures, allows one to define an effective local shape of a grain from any complex system made up of a distribution of arbitrarily shaped constituents. The method requires no prior knowledge of the original ensemble of grain size and shape. Here, we use this morphometric reconstruction method to predict transport and elastic properties of porous materials.

Kac [11] showed that the short time behaviour of the diffusion equation is governed by the additive measures ϕ, S, H and χ of a porous medium. In this section we follow [9] and show that a reconstructed material which honours these additive measures exhibits similar physical properties to the original system, for instance, to the Fountainebleau sandstone studied in the previous section 2. Use of the equivalent shape in effective medium formulations leads to excellent predictions of transport and elastic properties. Both the cases are considered where the equivalent grains are permeable solid grains (infinite contrast 1:0, e.g., sintered bead packs, sandstones, cement-based materials) and when the grains correspond to an inclusion, i.e., pore within a solid matrix (infinite contrast 0:1, e.g., closed cell foam, fractured materials, carbonate or basalt rock). The method of reconstructing the local shape at one porosity $\phi^{(\mathrm{recon})}$ and predicting from them the physical properties for all porosities ϕ is illustrated also for a sandstone sample.

Let us consider first a complex Boolean model, i.e., a random (Poisson) distribution of a heterogeneous mixture of five different spheroidal grains (five-grain system) defined by their three half axes (a, b, c). The system is made up of $p_1 = 40\%$ spheres ($a = b = c = 12$), $p_2 = 10\%$ oblate spheroids ($a = b = 24; c = 3$), $p_3 = 20\%$ oblate spheroids ($a = b = 18; c = 16/3$), $p_4 = 20\%$ prolate spheroids ($a = 24; b = c = 6\sqrt{2}$) and $p_5 = 10\%$ prolate spheroids ($a = 36; b = c = 4\sqrt{3}$). As the full distribution of grains is known, one can use the average $V_\nu = \sum_{j=1}^{5} p_j V_{\nu j}$ to derive the equivalent local grain shape for this ensemble. As shown in the previous section one can also predict V_ν from a single 3D snapshot at any porosity $\phi^{(\mathrm{recon})}$ of this complex mixture of grains and *reconstruct* an equivalent stochastic complex system. A single equivalent spheroidal grain (ROS model) defined by $a = b = 17.2, c = 5.8$ gives the best match to the local morphology V_ν.

Since physical properties of porous media are essentially influenced by the percolation behaviour of the pores let us compare first the percolation thresholds of the original five-grain system and of the reconstructed single-spheroidal-grain model. Interestingly, the percolation thresholds of the grain phase (p) and the inverse phase (i) respectively for the original five-grain system $\phi_c^{\mathrm{p}} = 0.173, \phi_c^{\mathrm{i}} = 0.0674$ and the equivalent model $\phi_c^{\mathrm{p}} = 0.183, \phi_c^{\mathrm{i}} = 0.0714$ are in good agreement. This result is an immediate consequence from the fact that the zero ϕ_0 of the Euler characteristic $\upsilon_3(\phi_0) = 0$ is an excellent estimate of the percolation threshold ϕ_c (see [37, 52, 66] for details). The percolation threshold ϕ_c of both phases is measured by determining $\phi_c(L)$ for various lattices sizes L and using the scaling ansatz: $\phi_c = \phi_c(L) + aL^{-b}$ [3, 67]. This ability to closely predict ϕ_c of *either* phase from an image at *a single* phase fraction $\phi^{(\mathrm{recon})}$ underlines the power of a morphological characterization and reconstruction based on integral geometric measures.

Now, one may numerically determine physical properties such as the conductance of the original system and of the reconstructed model. The conductivity calculation is based on a

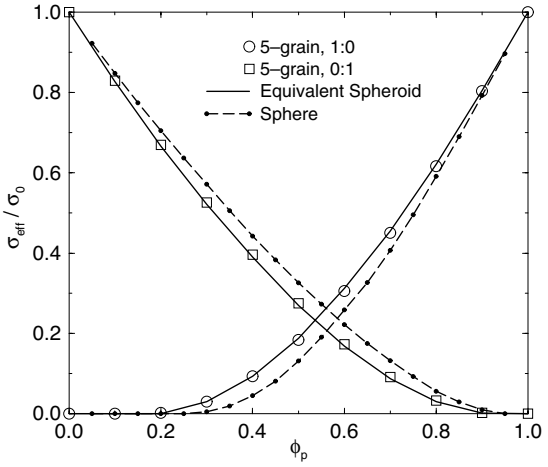

Figure 8. Effective conductivity at infinite contrast over particle fraction (ϕ_p) for the five-grain mixture and the equivalent single spheroidal grain model (from [9]). For any ϕ the largest difference is 0.007 between the original system and equivalent model. Predictions based on spherical grains are also given, which illustrates the importance of an accurate reconstruction of the morphology by using spheroids instead of spheres.

solution of the Laplace equation with periodic boundary conditions. In figure 8 the effective conductivity σ_{eff} of the five-grain system is compared with its equivalent stochastic model at infinite contrasts σ_p:$\sigma_i = 1$:0 and σ_p:$\sigma_i = 0$:1 The match of the equivalent single spheroidal grain ensemble to the original five-grain system is excellent in all cases and superior to a prediction based on spherical grains [68]. It is remarkable that one can generate the conductance curve *across all phase fractions for both the particle and inverse phase* of a complex Boolean system from a single image at $\phi_p^{(\text{recon})}$.

The predictions of the model reconstructions for the Fontainebleau sandstone at a scale of 120^3 are shown in figure 10. Of the reconstructions the Gaussian model, the only non-Boolean model, performs poorest. Of the Boolean models the model performing best is the $\text{ROS}^{(2)}$ model—as expected since it also matches the morphology best. However, the other one- and two-particle models still give a reasonable match, including the original IOS^{C} model, which was simply matched to the two-point correlation function (see also table 2). The OSC reconstruction consistently overestimates the conductivity of the Fontainebleau samples and works better in the intermediate porosity range (figures 10(b), (c)).

But does a reconstructed material which honours the additive measures also exhibit similar elastic properties to the original system? A finite element method [70] (FEM) is used to estimate the elastic properties of the original and equivalent granular systems. The bulk and shear moduli of the solid phase are set to those of quartz: $K_s = 37$ GPa and $G_s = 44$ GPa. In figure 9 the simulation results are shown for the original grain ensemble and for the equivalent stochastic match. The agreement is again excellent for both 1:0 and 0:1 contrasts. The morphology defined by the single equivalent grain captures the relevant structural aspects which determine the mechanical properties of the two-phase material at infinite contrast.

Calculating the material properties via reconstruction and numerical simulation over the full range of phase fractions gives excellent predictions but requires significant computational resources. To replace this intense computational effort with theoretical formulations would make the integral geometric technique more widely applicable. As an effective grain has been defined within the reconstruction method, one may consider an effective medium theory. For

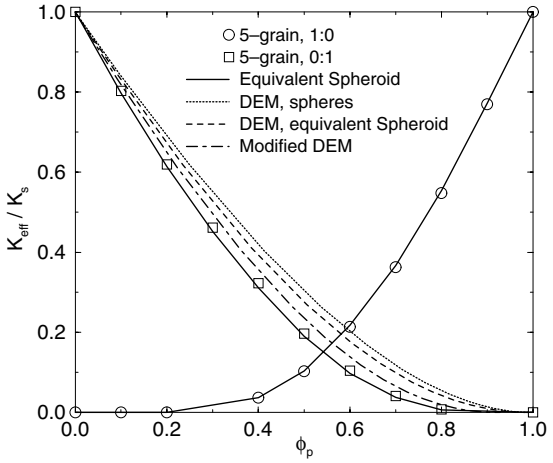

Figure 9. Bulk modulus over particle fraction ϕ_p for the heterogeneous five-grain and the equivalent grain pack (from [9]). For any ϕ the largest difference is 0.011 between the original system and equivalent model. DEM predictions are also given.

the elastic behaviour of porous materials two theories are often applied as they always lie within rigorous bounds; the self-consistent (SC) theory and the differential effective medium (DEM) theory [71]. The self-consistent SC theory requires defining the effective shape of both the inclusion (grain) phase *and* the inverse (pore) phase. The differential effective medium theory (DEM) treats the background phase as host medium at all phase fractions and only the morphology of the inclusion phase need be defined. As an effective shape for the inverse phase has not been defined yet, only DEM can be applied, which is a good model for materials with porous inclusions such as glass foams, vuggy carbonates and oceanic basalts [72] defined by

$$(1-\phi)\frac{\partial M^*_{\mathrm{DEM}}(\phi)}{\partial \phi} = [M_{\mathrm{s}} - M^*_{\mathrm{DEM}}(\phi)]S^*_{\mathrm{M}}, \tag{2}$$

where M_{s} and M_{DEM} are respectively the solid and effective moduli and S^*_{M} are shape-factors given in [73]. In most DEM formulations for materials with porous inclusions the equivalent pore shape S^*_{M} is either assumed to be spherical or is defined *a posteriori* to give a match to experimental data. Here, the effective pore shape derived from integral geometric considerations is used as an *a priori* prediction of S^*_{M} within the DEM formulation and compared to predictions based on spherical inclusions (see figure 9). The DEM with the amended shape leads to improved predictions. Conventional DEM can be modified to incorporate percolation behaviour by taking the material at the critical phase fraction as one of the constituents of the two-phase composite [74]. In figure 9 the prediction of this modified DEM model is shown using the equivalent local pore shape—the match is good.

In figure 11 the Fontainebleau sandstone data are compared to the reconstructions introduced in section 2 at the fixed resolution of 5.68 μm, namely the IOS model based on the two-point correlation function ($\mathrm{IOS}^{\mathrm{C}}$), the Boolean models based on the Minkowski functionals ($\mathrm{IOS}^{\mathrm{V}}$, $\mathrm{IOS}^{(2)}$, $\mathrm{ROS}^{(1)}$, $\mathrm{ROS}^{(2)}$), the Gaussian five-level intersection model [59] and the Boolean models based on the distribution of the covering radii (OSC, [57]). All models are reasonable predictions. Errors in predictions are at most $\pm 5\%$. Consistently the one-particle models based on the Boolean reconstruction perform very well. The IOS model based on the two-point correlation function shows a much weaker match to the elastic moduli of the Fontainebleau sandstone than the IOS model based on the Boolean reconstruction. The

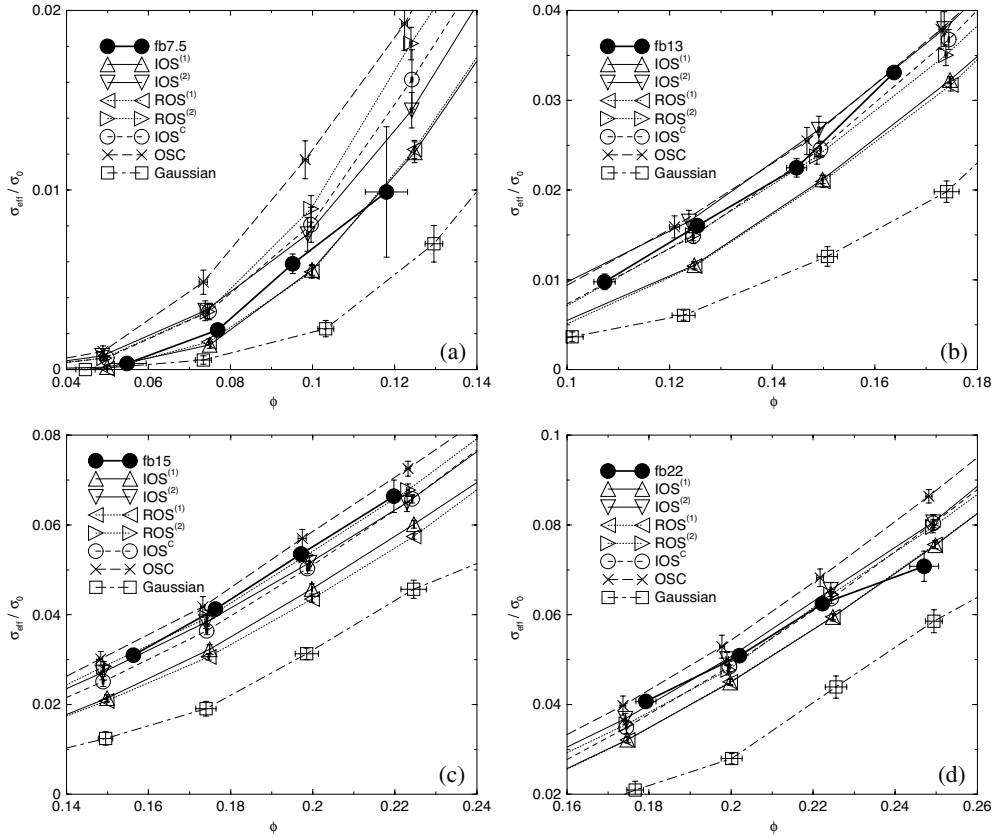

Figure 10. Comparison between the prediction for conductance of the matching Boolean and Gaussian models and the Fontainebleau sandstone data: (a) 7.5%, (b) 13%, (c) 15% and (d) 22%. The Gaussian model gives the worst match to the data over the full fractional range. Of the Boolean models, the OSC reconstruction gives a poor match to the data for the low porosity sample. The $\mathrm{ROS}^{(2)}$ model gives the best match, but the simple $\mathrm{IOS}^{\mathrm{C}}$ model performs well [69].

only difference is in the radii chosen (see table 2), and thus in the discretization of the model, and would scale out in the continuum limit. The Boolean matches based on two-particle reconstructions are surprisingly giving a poorer match than the one-particle models, despite the fact that the local morphology is matched better by these two-particle models. However, a sandstone is not generated by a Boolean process. This can lead to errors and is discussed and quantified in [69].

However, the morphometric approach has the potential to greatly improve predictions of complex multiphase materials based on effective medium methods. Let us consider an application in petroleum engineering, namely the prediction of the macropore or vuggy porosity within carbonate rocks. The presence of vugs can lead to enhanced recovery and improved flow properties. Current methods use shear modulus measurements from well logs to estimate the proportion of porosity due to vugs [76]. When interpreting the shear modulus measurements, vugs are assumed to be spherical in shape and predictions are based on the self-consistent effective medium (SC) theory [75, 76]. Microtomography was used to image a 4 cm $\times$ 4 cm $\times$ 1.5 cm reservoir carbonate core at the vug scale ($\simeq$50 μm) resolution [9]. 30 000 separate vugs are identified (see figure 12(a)), a broad size distribution

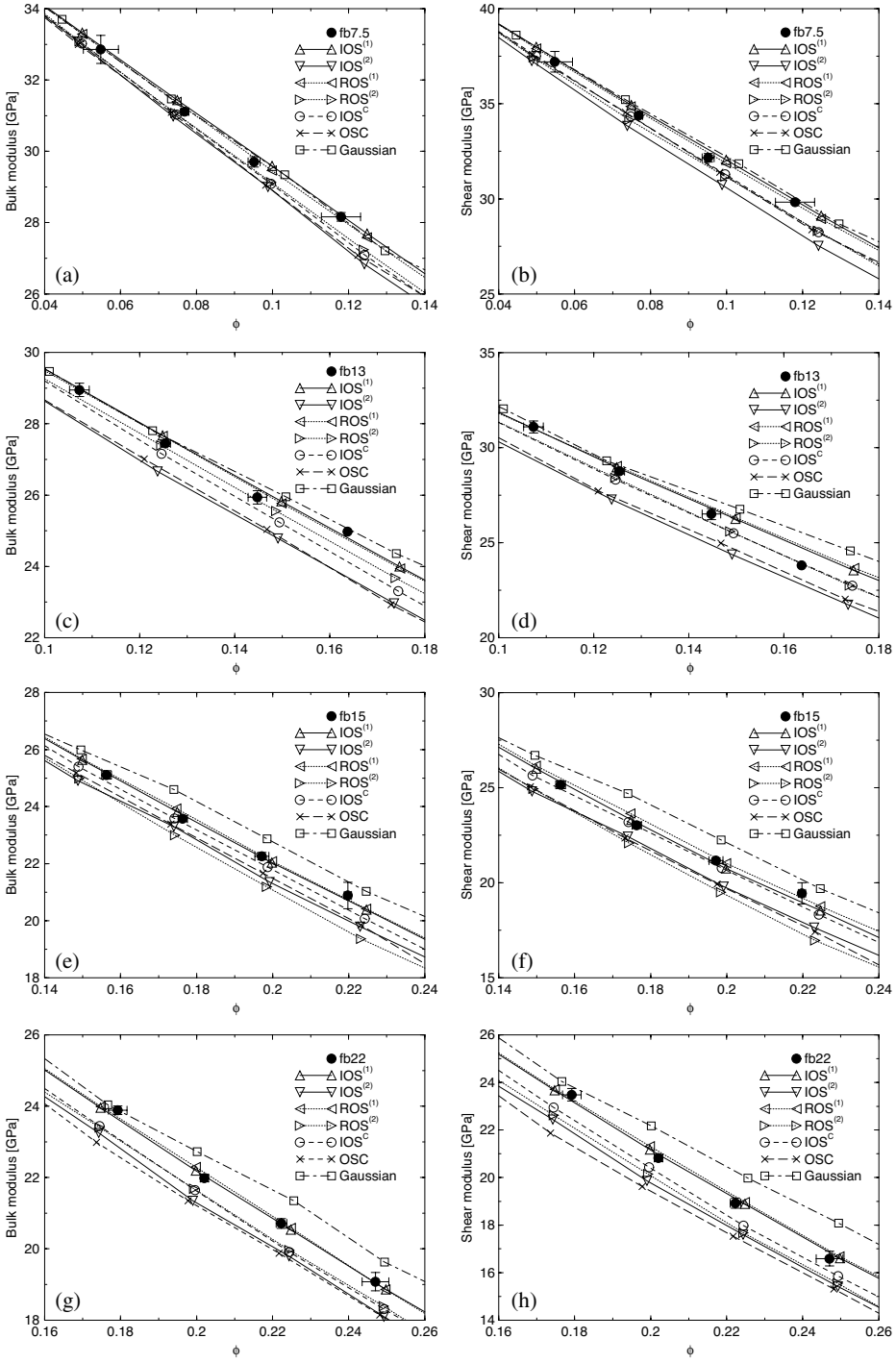

Figure 11. Image based calculations of the water saturated elastic moduli of the four Fontainebleau sandstone samples compared to Boolean and Gaussian reconstructions: (a), (b) 7.5%, (c), (d) 13%, (e), (f) 15% and (g), (h) 22%. The Fontainebleau sandstone data are corrected to represent a periodic 'infinite' sample.

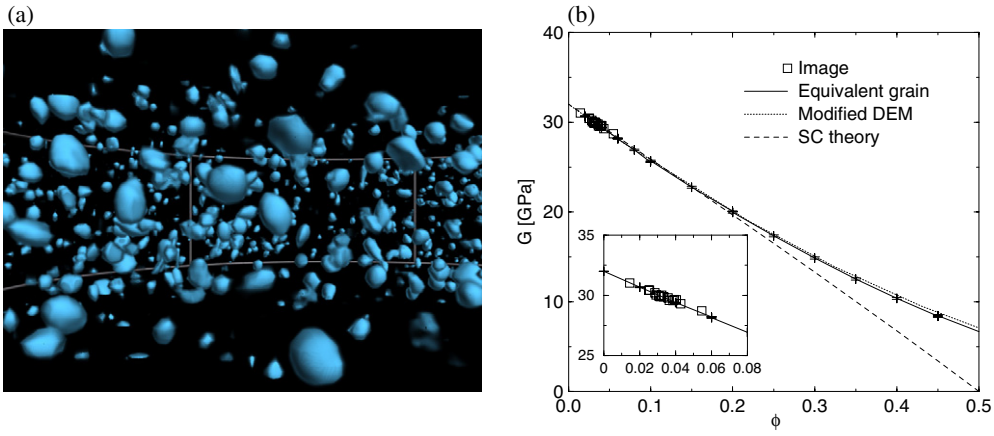

Figure 12. (a) Rendered 3D image showing the pore phase within a subset of the carbonate rock; (b) shear modulus derived from 3D tomogram, equivalent grain reconstruction, modified DEM theory and conventional SC theory (from [9]).

is measured and deviations from spherical shapes are found. As described in the previous section 2 one can derive from the single image the equivalent local grain morphology: $V_0^{\mathrm{im}} = 5.7 \times 10^6\ \mu\mathrm{m}^3$; $V_1^{\mathrm{im}} = 3.2 \times 10^4\ \mu\mathrm{m}^2$; $V_2^{\mathrm{im}} = 182\ \mu\mathrm{m}$. For this morphology a single equivalent grain does not match the V_ν^{im} as the isoperimetric inequality is violated. Searching through pairs of grains, one finds that a dual porosity system matches the measured V_ν: a 95%:5% mixture of prolate spheroidal pores with $a = 105\ \mu\mathrm{m}$; $b = c = 63\ \mu\mathrm{m}$ and $a = 701\ \mu\mathrm{m}$; $b = c = 164\ \mu\mathrm{m}$. FEM studies of shear modulus on 240^3 subsets of the original tomogram and the equivalent dual porosity mixture are shown in the inset of figure 12. The match is excellent.

The method for determining the vuggy porosity in carbonate rock formations is based on the deviation in the shear modulus from the characteristic behaviour of the shear modulus curve derived from SC theory [75, 76]. In figure 12 both the original and equivalent vug distribution is used to simulate the variation in shear modulus with vug porosity in the range $0 < \phi_{\mathrm{vug}} < 50\%$. Also shown is the error in using the SC theory for spherical vugs as the reference prediction for the shear modulus. The improved estimate of the shear modulus across all phase fractions based on modified DEM theory will lead to improved predictions of macropore fraction and ultimately oil recovery.

4. Thermodynamics of fluids in porous media

In the previous section 3 a powerful method is introduced to predict transport and elastic properties of porous media. The method is based on integral geometric measures and the Kac theorem for the spectrum of the Laplace operator. Also the thermodynamic behaviour of a liquid which is constrained by a geometrically complex pore such as the one shown in figure 13 may depend on the morphological measures of the pores, where the pore volume and surface area are only the simplest measures characterizing its shape. In [37, 84–86], for instance, the structure and phase behaviour of microemulsions could be explained assuming that the free energy, i.e., the effective Hamiltonian of the fluid domains on a mesoscopic scale, is given solely by the four Minkowski functionals. In [87] it was shown at least numerically that these four fundamental measures are indeed sufficient to describe the free energy of a hard-sphere

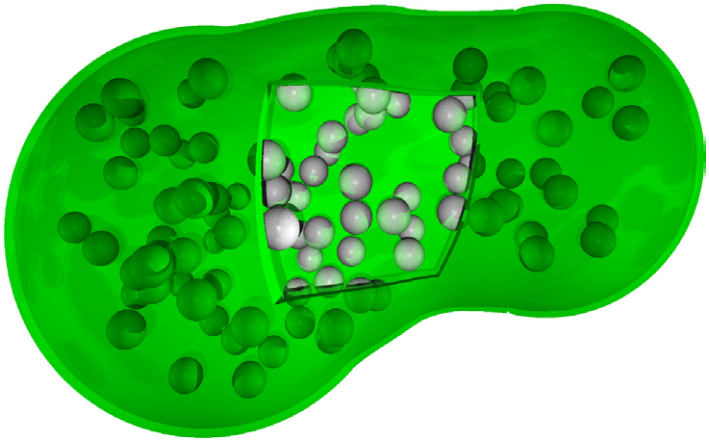

Figure 13. A hard sphere fluid confined by a complex shaped container S (image by courtesy of Peter König). In contrast to a complicated direct calculation of thermodynamic properties, equation (4) gives the grand potential Ω in terms of only four thermodynamic properties of the fluid, namely the pressure p, the surface tension σ and two bending rigidities κ and $\bar{\kappa}$ (see figure 14). Their energetically conjugated morphological quantities are the volume, the surface area, the integrated mean curvature and the Euler characteristic of the container S bounding the fluid. The Minkowski functionals $V_\nu[S]$ are therefore the only relevant 'extensive' thermodynamic variables related to the shape of the container S. They are readily available and easily allow the calculation of the grand canonical potential Ω for the fluid within pores of arbitrary size and shape.

fluid inside an arbitrarily shaped domain. Here, we follow the presentation of [87] and add new results in section 4.2 on capillary condensation, i.e., on the dependence of the liquid–vapour coexistence region on the shape of the pore space.

Although thermodynamics is built on extremely general assumptions its implications are far reaching and powerful. One basic building block is geometry which has a long history in thermodynamics and statistical physics of condensed matter. The formulation of thermodynamics in terms of differential forms [77], scaled-particle theory (SPT) for fluids [78], depletion forces [79] of colloids in biological cells [80] and density functional theory [81] (DFT) based on fundamental geometric measures [82] are only a few examples for the importance of a general geometric point of view on thermodynamic properties. In the following it is shown that not only transport and elastic properties but also thermodynamic quantities depend in a unique way on the geometry of the pore space, i.e., on the Minkowski functionals introduced in section 2.1.

4.1. Shape dependence of thermodynamic potentials

The grand potential $\Omega = \Omega[S; T, \mu]$ of a fluid depends on the temperature T and the chemical potential μ of the system, as well as on certain geometrical quantities which describe the shape of the container that bounds the system S (see figure 13). What are these thermodynamically relevant morphological parameters? One usually argues that every thermodynamic potential is an extensive quantity, which means that it scales linearly with the 'size' of the container S. By partitioning a large system into identical smaller subsystems one normally assumes that $\Omega[S; T, \mu]$ is proportional to the volume $V = V[S]$ of the system and uses as ansatz $\Omega[S; T, \mu] = \omega(T, \mu) \cdot V[S]$. The intensive quantity $\omega(T, \mu)$ is a thermodynamic property of the fluid and independent of the 'size' of the confining container of S. In the case of

the grand potential Ω it is the negative of the pressure $p(T, \mu)$ in the system. This simple ansatz however is only valid for infinite bulk, i.e. 'border-less' systems, as it ignores that a physical partitioning into finite systems induces changes in the grand potential due to the influence of the dividing wall. If S is bounded by a container, Ω depends on the shape of the container in a potentially complicated manner. However, in [87] it is shown that general considerations restrict this functional dependence on the shape to a linear combination of only four morphological measures, if all intrinsic length scales are small compared to the system 'size'. This finding is particularly important for depletion forces and torques [88] and for systems such as porous media [9] or biological cells [80], where fluids are confined by complex shaped compartments and where the dependence of thermodynamic quantities and transport properties on the shape of pores or cells has significant functional and biological consequences.

Let us focus on the dependence of the grand potential $\Omega[S]$ on the shape of the system S, i.e. let us regard $\Omega : S \to \mathbb{R}$ as a mapping from a container onto a real number. The actual form of this mapping is given by the type and state of the fluid under consideration and is a complicated integral over the phase space of the system, which can usually only be calculated approximately. However, one may impose the following three physical restrictions on this mapping.

(i) *Motion invariance.* Let $\mathcal{G}$ be the group of motions, namely translations and rotations in three dimensions. The action of $g \in \mathcal{G}$ on a domain S is denoted by gS. The grand potential $\Omega[gS] = \Omega[S]$ does not change for all g; i.e. the thermodynamic potential of a system must be independent of its location and orientation in space.

(ii) *Continuity.* If a sequence of convex sets $S_n \to S$ for $n \to \infty$, converges towards the convex set S, then the grand potential $\Omega[S_n] \to \Omega[S]$. Intuitively, this continuity property expresses the fact that an approximation of a convex domain by e.g. a convex polyhedron also yields an approximation of the thermodynamic potential $\Omega[S]$ by $\Omega[S_n]$.

(iii) *Additivity.* The grand potential of the union $S_1 \cup S_2$ of two domains S_i is the sum of the grand potential of the single domains subtracting the intersection

$$\Omega[S_1 \cup S_2] = \Omega[S_1] + \Omega[S_2] - \Omega[S_1 \cap S_2]. \tag{3}$$

This relation generalizes the common rule for the addition of an extensive quantity for two disjunct domains $S_1 \cap S_2 = \emptyset$ to the case of overlapping domains by subtracting the value of the thermodynamic quantity of the double-counted intersection. Note that the intersection $S_1 \cap S_2$ does not need to be a volume but can rather be an area or a line for adjacent containers S_i.

Naturally, the question arises about the most general form of a potential that satisfies these three conditions. The Hadwiger theorem [35, 38] (introduced in section 2.1 and already used for the reconstruction in section 2) states that every motion-invariant, conditional continuous and additive functional in three dimensions can be written as a linear combination of the volume $V_0 = \int_S \mathrm{d}^3\vec{x}$, the surface area $V_1 = \frac{1}{6}\int_{\partial S} \mathrm{d}^2\vec{x}$, the integrated mean curvature $V_2 = \frac{1}{3\pi}\int_{\partial S} H \ \mathrm{d}^2\vec{x}$ and the Euler characteristic $V_3 = \frac{1}{4\pi}\int_{\partial S} K \ \mathrm{d}A$ of the container wall. Therefore, one may write [37, 84–86]

$$\Omega[S] = -pV_0[S] + \sigma V_1[S] + \kappa V_2[S] + \bar{\kappa} V_3[S] \tag{4}$$

as a *complete* expression for the grand canonical potential. The pressure $p(T, \mu)$, the surface tension at the planar wall $\sigma(T, \mu)$ and the bending rigidities $\kappa(T, \mu)$ and $\bar{\kappa}(T, \mu)$ are properties of the fluid and the wall–fluid interaction, but are independent of the actual shape of the bounding wall. Note that this relation can be easily applied even to complex

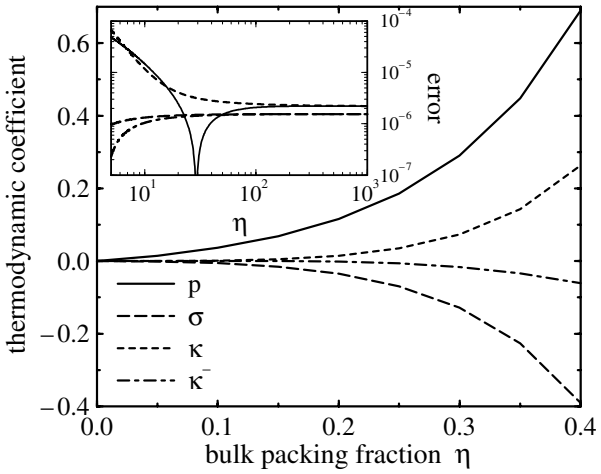

Figure 14. The expansion coefficients as defined in equation (4) of the grand potential of a hard-sphere fluid (from [87]). For each value of η, the four thermodynamic coefficients can be used to calculate thermodynamic quantities for arbitrarily shaped systems. The solid curve of the inset shows the relative error of the interfacial tension γ at a cylinder with radius R calculated using the thermodynamic coefficients at $\eta = 0.3$. This relative error is of the same order of magnitude as the relative numerical error of the contact sum-rules (dashed curve), indicating clearly that the very small deviation between the morphometric interfacial tension and that from a direct DFT calculation is a numerical error of our calculation.

shaped objects because the shape of S enters the thermodynamic potential only via the four simple morphometric measures V_ν, while the thermodynamic coefficients σ, κ and $\bar{\kappa}$ can be determined in a simpler geometry.

Thermodynamic quantities can be derived directly from the grand potential Ω and inherit a simple dependence on the shape of S by virtue of equation (4). For instance, the interfacial tension $\gamma = (\Omega + pV)/A$, which measures the total change in the grand potential per unit area introduced by the wall, can be evaluated using

$$\gamma = \sigma + \kappa \bar{H} + \bar{\kappa} \bar{K}, \tag{5}$$

where $\bar{H} = V_2/V_1$ and $\bar{K} = V_3/V_1$ are the averaged mean and Gaussian curvatures of the bounding wall. These geometrical quantities can be calculated from the principal radii of curvature R_1 and R_2 via $H = (1/R_1 + 1/R_2)/2$ and $K = 1/(R_1 R_2)$. Note that this further justifies the ansatz used in SPT [78, 90] for the interfacial tension and shows that the analytic dependence of the interfacial tension on the curvature [91] is a direct consequence of the additivity of the grand potential. No higher powers or derivatives of $\bar{H}$ or $\bar{K}$ contribute either to γ or to Ω.

In [87] the vanishing of higher powers of $\bar{H}$ and $\bar{K}$ in thermodynamic quantities such as Ω and γ was tested by considering a fluid of hard spheres of radius R bounded by a hard wall. The fluid was modelled via Rosenfeld's FMT [82]. The obtained thermodynamic coefficients of equation (4) are shown in figure 14 as functions of the packing fraction η of the fluid. From these coefficients one can obtain values for the surface tension γ for various geometries. In the inset of figure 14 the relative error (full curve), i.e., the difference of the interfacial tension γ of a hard-sphere fluid from the expression given by equation (5), is shown with packing fraction $\eta = 0.3$ at a cylinder with radius R as calculated with the thermodynamical coefficients compared to that obtained directly from DFT. This error can be compared to the numerical relative error for a sum rule [89, 90] (dashed curve), which gives an estimate for

the accuracy of our DFT data. Both errors are of the same order of magnitude such that our numerical data are in agreement with the prediction of equation (4). Thus, the surface tension contains, beside a constant term, only contributions linear in the mean and Gaussian curvature of the container.

The assumption that the grand potential of a fluid is motion invariant, continuous and additive allows an expansion of thermodynamic quantitities in terms of only four simple morphological functionals. As a consequence, curvature expansions exactly terminate after linear terms in mean and Gaussian curvature. This observation allows a calculation of thermodynamic quantities for complex shaped objects with a greatly reduced effort in comparison to direct methods. The ideas presented here and in [87] for the hard-sphere fluid can also be applied to fluids with short-ranged interactions provided that internal length scales are small compared to typical features of the container. However, the arguments cannot be applied, for instance, to critical phenomena, or if long ranged fluid–fluid or fluid–wall interactions are considered or if wetting or drying phenomena [83] occur at the wall, as intrinsic lengths in such systems have a macroscopic size.

4.2. Capillary condensation

Another example where integrals of curvature naturally occur is the phase behaviour of fluids in a porous medium. An important phenomenon is capillary condensation, i.e., the reduction of the critical point and the shift of the equilibrium chemical potential and the equilibrium pressure towards lower values due to the interaction of the fluid with a substrate. In other words, a liquid starts to boil at a higher temperature if it is enclosed by a small box. This phenomenon is quite general and can be explained straightforwardly using a simple geometric configuration. Consider, for instance, two plates of distance D; then the grand canonical potentials Ω of a homogeneous vapour and liquid phase are given by $\Omega_{\mathrm{g}} = -pV + 2A\gamma_{\mathrm{sg}}$ and $\Omega_{\mathrm{l}} = -p^{+}V + 2A\gamma_{\mathrm{sl}}$, respectively. Here, p is assumed to be the unaltered bulk vapour pressure whereas p^{+} is the pressure of a metastable fluid phase stabilized by the substrate. A is the surface area of the substrate and γ denotes the surface tension between the solid substrate and the fluid phases. Thermodynamic equilibrium requires $\Omega_{\mathrm{g}} = \Omega_{\mathrm{l}}$ and one obtains the well known Kelvin equation

$$p - p^{+} = 2\frac{\gamma_{\mathrm{sg}} - \gamma_{\mathrm{sl}}}{D} \simeq 2\frac{\gamma_{\mathrm{lg}}}{D} > 0 \tag{6}$$

for the coexistence of a fluid and a vapour phase between two planar walls of distance D. Thus, if the distance of the walls becomes small the pressure difference $p - p^{+}$ forces a vapour to condense while it remains gaseous in the bulk outside the slit. But what happens in a real porous substrate?

Using a density functional theory for fluids in a porous medium one can calculate the shift of the critical point and of the boiling temperature in terms of geometric measures of the porous substrate. The present analysis is based on a simple version of density functional theory for one-component fluids which consist of particles with a rotationally symmetric pair interaction potential $w(r)$. Within this approach the interaction potential $w(r) = w_{\mathrm{s}}(r) + w_{\mathrm{l}}(r)$ is split into a short-ranged repulsive part $w_{\mathrm{s}}(r)$ and a long-ranged attractive part $w_{\mathrm{l}}(r)$ [81]. The interaction between the fluid and the substrate is taken into account by a potential $V_S(\vec{r})$. The grand canonical density functional reads

$$\Omega[\rho(\vec{r})] = \int_V \mathrm{d}^3 r \left[f_h(\rho(\vec{r})) - \mu\rho(\vec{r}) + \rho(\vec{r}) V_S(\vec{r}) \right] + \tfrac{1}{2} \int_V \mathrm{d}^3 r \int_V \mathrm{d}^3 r' w_{\mathrm{l}}(\|\vec{r} - \vec{r}'\|)\rho(\vec{r})\rho(\vec{r}') \tag{7}$$

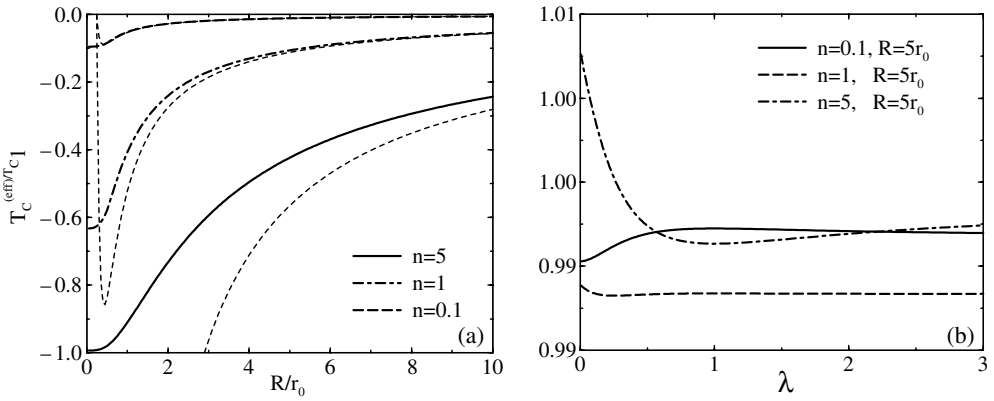

Figure 15. Shift of the critical point in a porous medium formed by overlapping (a) spheres of size R at volume density $n = m_0\rho$ and (b) ellipsoids of aspect ratio λ. For Poisson distributed grains K the structure function in equation (9) reads $S(r) = \mathrm{e}^{-nv+nV(K\cap K_{\vec{r}})}$. For fixed volume fraction $\phi = \mathrm{e}^{-n}$ (porosity) the critical point still depends on the aspect ratio λ and on the range of the interaction potential R/r_0 relative to the radius of the spheres. The relevant regime for physical applications of the approximation is $R/r_0 \gg 1$. (b) Even if the volume fraction $\phi = \mathrm{e}^{-n}$ (porosity) and additionally the mean surface area $8nm_1/m_0$ per volume are fixed for a porous medium, one finds a dependence of the phase transition temperature on the shape of the pore. Without taking into account the curvature contribution the critical point shift is given by $1 - T_c^{(\mathrm{eff})}/T_c = 8nm_1/m_0\gamma_0/w^{(0)}$, i.e., by $-0.011\,25$ ($n = 0.1$, $R = 10$, solid curve), -0.1125 ($n = 1$, $R = 10$, dashed curve), -0.5625 ($n = 5$, $R = 10$, dot–dashed curve).

where V is the volume of the sample, $\rho(\vec{r})$ the number density of the fluid particles at $\vec{r} = (x, y, z)$, $r = |\vec{r}|$, and $f_h(\rho)$ is the reference free energy of a system determined by the short-ranged contribution to the interaction potential $w_s(r)$. For these calculations let us adopt the Carnahan–Starling expression $f_h(\rho) = k_B T\rho\{\ln(\rho\lambda^3) - 1 + \frac{4\eta-3\eta^2}{(1-\eta)^2}\}$, where λ is the thermal de Broglie wavelength and $\eta = \frac{\pi}{6}\rho r_0^3$ the packing fraction.

Within this density functional approach the equilibrium density $\rho^{(\mathrm{eq})}(\vec{r})$ of the fluid inside the porous medium minimizes the functional $\Omega\left[\rho(\vec{r})\right]$ in equation (7) which yields the grand canonical potential $\Omega = \Omega[\rho^{(\mathrm{eq})}(\vec{r})]$. The equilibrium profile depends not only on the temperature T, the chemical potential μ, and the substrate potential $V_S(\vec{r})$ but also on the position $\vec{r}$ inside the pores. Nevertheless, one may show that the shift in the critical point and, accordingly, the difference in the equilibrium pressures of the fluid bulk phases is given by the expansion

$$(p - p^+)V = \sum_{\nu=1}^{3} h_\nu[w(r)]V_\nu + \frac{\kappa}{2}\int H^2\,\mathrm{d}\mathcal{S} + \cdots \tag{8}$$

with coefficients h_ν depending on the system parameters and the interaction potential $w(r)$ of the fluid particles. For a slit of parallel flat walls of distance D one obtains $V_2 = V_3 = H^2 = 0$ and recovers immediately the result given by equation (6). In other words, relation (8) generalizes Kelvin's equation, which turns out to be the first term in a curvature expansion of the pressure difference $p - p^+$. The density functional approach also gives expressions for the coefficients $h_\nu[w(r)]$, i.e., for surface tensions γ_{sg} and bending rigidities in terms of the microscopic interaction potential $w(\vec{r})$. Assuming that the equilibrium fluid density $\rho^{(\mathrm{eq})}(\vec{r}) \equiv \rho$ is constant inside the pores one can derive an alternative expression to equation (8) based on the structure function $S(r)$ of the porous substrate $\mathcal{K}$ (see section 2.3). One finds for

the shift $\delta T_c = (T_c - T_c^0)/T_c^0$ of the critical point (see figure 15)

$$\delta T_c = \int_V \mathrm{d}^3\vec{r}\, \frac{w_1(r)}{w^{(0)}} \mathrm{e}^{n\nu}(S(0) - S(r)). \tag{9}$$

The structure function $S(r)$ of a porous substrate can be measured by scattering experiments independently from a calorimetric determination of the critical point, so that a test is possible of the relation (9) between the morphology and the thermodynamics of a porous material. Of course, the expression is based on the assumption of a homogeneous density of the fluid inside the pores and has to be improved by applying the concept of parallel surfaces as indicated in section 2.5. However, equation (9) is an example for a structure–property relation scientists and engineers are looking for. Expanding the structure function $S(r)$ in powers of the distance r [92–94]

$$S(r) = \frac{V_0(\mathcal{K})}{V} - \frac{3r}{4}\frac{V_1(\mathcal{K})}{V} - \frac{r^3}{32}\frac{V_3(\mathcal{K})}{V} + \frac{r^3}{32V}\int_{\partial\mathcal{K}} H^2\,\mathrm{d}S + \mathcal{O}(r^5) \tag{10}$$

one recovers an expression in terms of Minkowski functionals V_ν of the porous structure. Since the expansion (10) is only valid for sharp interfaces, the contribution proportional to the mean curvature H vanishes and the bending rigidities κ and $\bar{\kappa}$ are identical, which is not the case for non-constant density profiles $\rho^{(\mathrm{eq})}(\vec{r})$ inside the pores. Inserting (10) in equation (9) one recovers a curvature expansion for the critical point shift

$$\delta T_c = h_1[w(r)]\frac{V_1[S]}{V} + h_2[w(r)]\frac{V_2[S]}{V} \tag{11}$$

analogous to the generalized Kelvin equation (8) with explicitly given coefficients

$$h_1[w(r)] = \pi\int_0^\infty \mathrm{d}r\, r^3 w_1(r), \qquad h_2[w(r)] = \frac{\pi}{24}\int_0^\infty \mathrm{d}r\, r^5 w_1(r). \tag{12}$$

Equation (11) is certainly not valid near the critical point because the thickness of a fluid adsorption layer at the substrate wall is determined by the correlation length $\xi(T)$ which becomes large at T_c. Instead of the critical point shift $\delta T_c \sim D^{-1}$ as implied by equation (11) for a fluid between walls of distance D, one expects $\delta T_c \sim D^{-2}$ if density inhomogeneities of size ξ are taken into account.

Curvature expansions such as in equations (4), (5), (8), and (10) are quite common in physics and very useful for practical purposes. Integral geometry and Minkowski functionals provide precisely the mathematical backbone and technical calculus for physical applications of curvature measures. In section 2.1, for instance, the geometric functionals V_ν are given for the Boolean model, so that explicit expressions for the phase behaviour of fluids in porous media modelled by overlapping grains can be derived. Although expression (9) has to be improved it indicates a direction for future work, namely the prediction of thermodynamic properties of materials when the morphology is known.

The complicated pore structure of an interconnected three-dimensional network of capillary channels of nonuniform sizes and shapes distinguishes a porous medium from any other solid or planar substrate. The connection of the two main features of fluids in porous media, namely morphology and interfacial effects such as surface energies and wettability, may help in future studies to understand the influence of the random geometric structure on phase behaviour and transport properties, which are inherently determined by inhomogeneous spatial structures on all length scales of the porous material.

5. Summary

Foams, gels and porous structures become increasingly important for technological applications due to their special material properties as spatially structured matter. The physical

properties depend crucially on the morphology, i.e., on shape and connectivity of the pores. The knowledge, for instance, of the dependence of percolation thresholds on the distribution and shape of pores is necessary for many applications ranging from oil recovery to conductivities of modern materials.

Integral geometric measures, i.e., Minkowski functionals of the spatial structure, proved to be structural quantities which are important for many physical properties of heterogeneous materials. For instance, in section 3 it was shown that completely different porous media exhibit very similar conductivities and elastic moduli as long as the structures have the same Minkowski functionals. In section 4 we could even show that thermodynamic quantities such as surface energies of a hard sphere fluid in an arbitrarily complex shaped pore depend only linearly on the Minkowski functionals of the pore space. Thus, morphological measures such as the Minkowski functionals are not only useful to quantitatively characterize the shape and to optimally reconstruct spatially complex structures, but also to accurately predict fluid properties in porous media.

Acknowledgments

It is a great pleasure to thank Mark Knackstedt, Peter König and Roland Roth for fruitful collaborations and stimulating discussions. Financial support by the DFG under grants Me1361/7 (1-2) within the priority programme 'Wetting and structure formation at interfaces' and the DAAD (PPP Australien) are acknowledged.

References

[1] Sahimi M 2003 *Heterogeneous Materials* vol 1 (New York: Springer)
[2] Torquato S 2002 *Random Heterogeneous Materials: Microstructure and Macroscopic Properties* (New York: Springer)
[3] Sahimi M 1995 *Flow and Transport in Porous Media and Fractured Rock* (Weinheim: VCH)
[4] Dullien F A L 1992 *Porous Media, Fluid Transport and Pore Structure* (San Diego, CA: Academic)
[5] Mecke K R 2000 *Additivity, Convexity, and Beyond: Applications of Minkowski Functionals in Statistical Physics* (*Springer Lecture Notes in Physics* vol 554) (Berlin: Springer) pp 111–84
[6] Stoyan D and Mecke K 2004 *The Boolean Model from Matheron up to Today* ed J Serra, at press (Invited contribution to the memorial volume honoring Georges Matheron)
[7] Arns C H, Knackstedt M A, Pinczewski W V and Mecke K 2001 Euler-Poincaré characteristics of classes of disordered media *Phys. Rev.* E **63** 31112:1–13
[8] Arns C H, Knackstedt M A and Mecke K 2002 *Characterising the Morphology of Disordered Materials* (*Springer Lecture Notes in Physics* vol 600) (Berlin: Springer) pp 40–78
[9] Arns C H, Knackstedt M A and Mecke K 2003 *Phys. Rev. Lett.* **91** 215506
[10] Arns C H, Knackstedt M A and Mecke K 2004 Characterisation of irregular spatial structures by parallel sets and integral geometric measures *Colloids Surf.* A **241** 351–72
[11] Kac M 1966 *Am. Math. Mon.* **73** 1
[12] Berk N F 1991 Scattering properties of the leveled-wave model of random morphologies *Phys. Rev.* A **44** 5069–79
[13] Teubner M 1991 Level surfaces of Gaussian random fields and microemulsions *Europhys. Lett.* **14** 403–8
[14] Cahn J W 1965 Phase separation by spinodal decomposition in isotropic systems *J. Chem. Phys.* **42** 93–9
[15] Berk N F 1987 Scattering properties of a model bicontinuous structure with a well defined length scale *Phys. Rev. Lett.* **58** 2718–21
[16] Knackstedt M A and Roberts A P 1996 Morphology and macroscopic properties of conducting polymer blends *Macromolecules* **29** 1369–71
[17] Roberts A P and Knackstedt M 1995 Mechanical and transport properties of model foamed solids *J. Mater. Sci. Lett.* **14** 1357–9
[18] Gibson L and Ashby M 1988 *Cellular Solids: Structure and Properties* (Oxford: Pergamon)
[19] Stoyan D, Kendall W S and Mecke J 1995 *Stochastic Geometry and its Applications* (Chichester: Wiley)

[20] Mecke K R and Stoyan D (ed) 2000 *Statistical Physics and Spatial Statistics—The Art of Analyzing and Modeling Spatial Structures and Pattern Formation* (*Springer Lecture Notes in Physics* vol 554) (Berlin: Springer)
[21] Mecke K R and Stoyan D (ed) 2002 *Morphology of Condensed Matter—Physics and Geometry of Spatially Complex Systems* (*Springer Lecture Notes in Physics* vol 600) (Berlin: Springer)
[22] Serra J (ed) 1992 *Image Analysis and Mathematical Morphology: Theoretical Advances* vol 2 (New York: Academic)
[23] Joshi M 1974 A class of stochastic models for porous materials *PhD Thesis* University of Kansas, Lawrence
[24] Adler P, Jacquin C and Thovert J-F 1992 The formation factor of reconstructed porous media *Water Resources Res.* **28** 1571–6
Adler P M, Jacquin C G and Quiblier J A 1990 *Int. J. Multiphase Flow* **16** 691
[25] Fredrich J T, Greaves K H and Martin J W 1993 Pore geometry and transport properties of Fontainebleau sandstone *Int. J. Rock Mech. Min. Sci.* **30** 691–7
[26] Roberts N, Reed M and Nesbitt G 1997 Estimation of the connectivity of a synthetic porous medium *J. Microsc.* **187** 110–8
[27] Yeong C L Y and Torquato S 1998 Reconstructing random media *Phys. Rev.* E **57** 495–506
Yeong C L Y and Torquato S 1998 Reconstructing random media: ii. Three-dimensional media from two-dimensional cuts *Phys. Rev.* E **58** 224–33
[28] Scheidegger A 1974 *The Physics of Flow through Porous Media* (Toronto: University of Toronto Press)
[29] Lohmann G 1998 *Volumetric Image Analysis* (Chichester: Wiley)
[30] Ohser J and Mücklich F 2000 *Statistical Analysis of Materials Structures* (Chichester: Wiley)
[31] Manwart C, Torquato S and Hilfer R 2000 Stochastic reconstruction of sandstones *Phys. Rev.* E **62** 893–9
[32] Roberts A P and Torquato S 1999 Chord distribution functions of three-dimensional random media: approximate first-passage times of Gaussian processes *Phys. Rev.* E **59** 4953–61
[33] Hilfer R 1958 *Transport and Relaxation Phenomena in Porous Media* (*Advances in Chemical Physics* vol XCII) (New York: Wiley) pp 299–424
[34] Rosenfeld A 1976 *Digital Picture Processing* (New York: Academic)
[35] Hadwiger H 1957 *Vorlesungen über Inhalt, Oberfläche und Isoperimetrie* (Berlin: Springer)
[36] Santaló L A 1976 *Integral Geometry and Geometric Probability* (Reading, MA: Addison-Wesley)
[37] Mecke K R 1994 *Integralgeometrie in der Statistischen Physik* (Frankfurt: Verlag Harri Deutsch)
[38] Mecke K R 1998 Integral geometry and statistical physics *Int. J. Mod. Phys.* B **12** 861–99
[39] Mecke K R 1997 Morphology of spatial patterns: porous media, spinodal decomposition, and dissipative structures *Acta Phys. Pol.* B **28** 1747–82
[40] Mecke K R 1996 Morphological characterization of patterns in reaction-diffusion systems *Phys. Rev.* E **53** 4794–800
[41] Becker J, Grün G, Seemann R, Jacobs K, Mecke K and Blossey R 2003 Complex dewetting scenarios captured by thin film models *Nat. Mater.* **2** 59–64
[42] Mecke K R and Sofonea V 1997 Morphology of spinodal decomposition *Phys. Rev.* E **56** R3761–4
[43] Sofonea V and Mecke K R 1999 Morphological characterization of spinodal decomposition kinetics *Eur. Phys. J.* B **8** 99–112
[44] Kerscher M, Mecke K, Schmalzing J, Beisbart C, Buchert T and Wagner H 2001 Morphological fluctuations of large-scale structure: the PSCz survey *Astron. Astrophys.* **373** 1–11
[45] Kerscher M, Mecke K, Schücker P and and the REFLEX collaboration 2001 Minkowski functionals of the REFLEX cluster catalogue *Astron. Astrophys.* **377** 1–16
[46] Jacobs K, Herminghaus S and Mecke K R 1998 Thin liquid polymer films rupture via defects *Langmuir* **14** 965–9
[47] Herminghaus St, Jacobs K, Mecke K, Bischof J, Frey A, Ibn-Elhaj M and Schlagowski St 1998 Spinodal dewetting in liquid crystal and liquid metal films *Science* **282** 916–9
[48] Jacobs K, Seemann R and Mecke K R 2000 *Dynamics of Dewetting and Structure Formation in Thin Liquid Films* (*Springer Lecture Notes in Physics* vol 554) (Berlin: Springer) pp 72–91
[49] Brodatzki U and Mecke K 2002 Simulating stochastic geometries: morphology of overlapping grains *Comput. Phys. Commun.* **147** 218–21
[50] Mecke K R 2001 Exact moments of curvature measures in the Boolean model *J. Stat. Phys.* **102** 1343–81
[51] Hyde S T, Barnes I S and Ninham B W 1990 Curvature energy of surfactant interfaces confined to the plaquettes of a cubic lattice *Langmuir* **6** 1055–62
[52] Mecke K and Seyfried A 2002 Strong dependence of percolation thresholds on polydispersity *Europhys. Lett.* **58** 28–34
[53] Dunsmuir J H, Ferguson S R and D'Amico K L 1991 Design and operation of an imaging X-ray detector for microtomography *IOP Conf. Ser.* **121** 257–61

[54] Spanne P, Thovert J F, Jacquin C J, Lindquist W B, Jones K W and Adler P M 1994 Synchotron computed microtomography of porous media: topology and transports *Phys. Rev. Lett.* **73** 2001–4
[55] Flannery B P, Deckman H W, Roberge W G and D'Amico K L 1987 Three-dimensional x-ray microtomography *Science* **237** 1439–44
[56] Lindquist W B and Venkatarangan A 1999 Investigating 3D geometry of porous media from high resolution images *Phys. Chem. Earth* A **25** 593–9
Lindquist W B, Venkatarangan A, Dunsmuir J and Wong T F 2000 Pore and throat size distributions measured from synchrotron x-ray tomographic images of Fontainebleau sandstones *J. Geophys. Res.* B **105** 21509–27
[57] Thovert J-F, Yousefian F, Spanne P, Jacquin C G and Adler P M 2001 *Phys. Rev.* E **63** 061307
[58] Sok R M, Knackstedt M A, Sheppard A P, Pinczewski W, Lindquist W B, Venkatarangan A and Paterson L 2002 *Transport Porous Media* **46** 345
[59] Roberts A P 1997 Statistical reconstruction of three-dimensional porous media from two-dimensional images *Phys. Rev.* E **56** 3203–12
[60] Quiblier J 1984 A new three-dimensional modeling technique for studying porous media *J. Colloid Interface Sci.* **98** 84–102
[61] Teubner M and Strey R 1987 Origin of the scattering peak in microemulsions *J. Chem. Phys.* **87** 3195–200
[62] Bakke S and Oren P E 1997 3-D pore-scale modelling of sandstones and flow simulations in the pore networks *SPE J.* **2** 136–49
[63] Øren P E, Bakke S and Arntzen O J 1998 Extending predictive capabilities to network models *SPE J.* **3** 324–36
[64] Mecke K 2002 The shapes of parallel surfaces: porous media, fluctuating interfaces and complex fluids *Physica* A **314** 655–62
[65] Øren P E and Bakke S 2002 Process based reconstruction of sandstones and prediction of transport properties *Transport Porous Media* **46** 311–43
[66] Mecke K R and Wagner H 1991 Euler characteristic and related measures for random geometric sets *J. Stat. Phys.* **64** 843
[67] Stauffer D and Aharony A 1994 *Introduction to Percolation Theory* (London: Taylor and Francis)
[68] Coelho D, Thovert J-F and Adler P M 1997 *Phys. Rev.* E **55** 1959
[69] Arns C H 2002 The influence of morphology on physical properties of reservoir rocks *PhD Thesis* University of New South Wales
[70] Garboczi E J and Day A R 1995 *J. Mech. Phys. Solids* **43** 1349
[71] Berryman J G 1995 Mixture theories for rock properties *A Handbook of Physical Constants* (Washington, DC: American Geophysical Union) pp 205–28
[72] Berge P A, Berryman J G and Bonner B P 1993 *Geophys. Res. Lett.* **20** 2619
[73] Berryman J G 1980 *J. Acoust. Soc. Am.* **69** 416
[74] Mukerji T, Berryman J, Mavko G and Berge P 1995 *Geophys. Res. Lett.* **22** 555
[75] Ramamoorthy R, Johnson D L and Murphy W F M III 1999 Porosity estimation method in carbonate rock *US Patent Specification* 5,869,755
[76] Ramakrishnan T S, Ramamoorthy R, Fordham E, Schwartz L, Herron M, Saito N and Rabaute A 2001 *Technical Report*, SPE Paper 71704
[77] Frankel Th 1997 *The Geometry of Physics: An Introduction* (Cambridge: Cambridge University Press)
[78] Reiss H, Frisch H L, Helfand E and Lebowitz J L 1960 *J. Chem. Phys.* **32** 119
[79] Roth R, Evans R and Dietrich S 2000 *Phys. Rev.* E **62** 5360
[80] Ellis R J 2001 *Trends Biochem. Sci.* **26** 597
[81] Evans R 1992 Density functionals in the theory of nonuniform fluids *Fundamentals of Inhomogeneous Fluids* ed D Henderson (New York: Dekker) pp 85–175
also Evans R 1979 The nature of the liquid–vapour interface and other topics in the statistical mechanics of non-uniform, classical fluids *Adv. Phys.* **28** 143–200
[82] Rosenfeld Y 1989 *Phys. Rev. Lett.* **63** 980
[83] Evans R, Roth R and Bryk P 2003 *Europhys. Lett.* **62** 815
[84] Likos C N, Mecke K R and Wagner H 1995 Statistical morphology of random interfaces in microemulsions *J. Chem. Phys.* **102** 9350–61
[85] Mecke K R 1996 Morphological model for complex fluids *J. Phys.: Condens. Matter* **8** 9663–7
[86] Mecke K R 1998 Morphological thermodynamics of composite media *Fluid Phase Equilib.* **150/151** 591–8
[87] König P-M, Roth R and Mecke K 2004 Morphological thermodynamics *Phys. Rev. Lett.* **93** 160601
[88] Roth R, van Roij R, Andrienko D, Mecke K R and Dietrich S 2002 Entropic torque *Phys. Rev. Lett.* **89** 88301–4
[89] Henderson J R 1983 *Mol. Phys.* **50** 741
[90] Bryk P, Roth R, Mecke K R and Dietrich S 2003 *Phys. Rev.* E **68** 031602

[91] Bryk P, Roth R, Mecke K R and Dietrich S 2003 Hard-sphere fluids in contact with curved substrates *Phys. Rev.* E **68** 031602
[92] Porod G 1951 *Kolloid Z.* **124** 83
Porod G 1952 *Kolloid Z.* **125** 21
Porod G 1952 *Kolloid Z.* **125** 108
Kirste R and Porod G 1962 *Z. Polym.* **184** 1
[93] Ciccariello S 1985 *Acta Crystallogr.* A **41** 560
Ciccariello S, Cocco G, Benedetti A and Enzo S 1981 *Phys. Rev.* B **23** 6474
[94] Teubner M 1990 Scattering from two-phase random media *J. Chem. Phys.* **92** 4501–7